**Key Points:**
- Duration of one-layer ice cloud coverage increases up to 5 days before the Madden-Julian Oscillation (MJO) passage
- Neglecting longwave scattering leads to a 3.5 to 5.0 W m$^{-2}$ overestimation of the outgoing longwave radiation (OLR)
- Neglecting longwave scattering leads to a less sharp heating gradient from cloud base to cloud top

**Correspondence to:**
T. Ren,
tr7585@tamu.edu

# Impact of Cloud Longwave Scattering on Radiative Fluxes Associated With the Madden-Julian Oscillation in the Indian Ocean and Maritime Continent

**Tong Ren[1]** [iD], **Ping Yang[1]**, **Courtney Schumacher[1]** [iD], **Xianglei Huang[2]** [iD], **and Wuyin Lin[3]**

[1]Department of Atmospheric Sciences, Texas A&M University, College Station, TX, USA, [2]Department of Climate and Space Sciences and Engineering, University of Michigan, Ann Arbor, MI, USA, [3]Brookhaven National Laboratory, Brookhaven, NY, USA

**Abstract** Previous studies suggested that cloud longwave radiation contributes to the development and maintenance of the Madden-Julian Oscillation (MJO) and model-based convection is highly sensitive to the radiation scheme. However, currently used radiation schemes do not take cloud longwave scattering into account, resulting in an overestimation of the outgoing longwave radiation (OLR) and an underestimation of the downward longwave flux at the surface. We use combined active and passive satellite cloud property retrievals to quantify the one-layer cloud OLR and heating rate (*HR*) biases introduced by neglecting cloud longwave scattering in the Indian Ocean and Maritime Continent in the context of MJO, with a focus on its phases 3, 5, and 6. The results show that the satellite-detected one-layer cloud area consists primarily of ice clouds, particularly during the boreal winter in the 4-year study period. An increased ice cloud area fraction of one-layer cloud groups is present up to 5 days before the onset of MJO events. If longwave scattering is neglected, the composite mean OLR overestimation over the one-layer ice cloud area from 5 days before to 4 days after the MJO passage is approximately 3.5 to 5.0 W m$^{-2}$. Neglecting longwave scattering also leads to a *HR* underestimation at cloud base and an overestimation at cloud top, making the base-to-top heating gradient less sharp at the cloud-resolving scale.

## 1. Introduction

The Madden-Julian Oscillation (MJO; Madden & Julian, 1971, 1972), an intraseasonal variability mode over the tropics, is closely related to both tropical and extratropical weather and climate (Stan et al., 2017; Zhang, 2005, 2013). Numerous studies have suggested that cloud-radiation interaction (CRI) plays an important role in regulating tropical intraseasonal variability, such as the MJO (e.g., Arnold & Randall, 2015; Crueger & Stevens, 2015; Del Genio & Chen, 2015; Hu & Randall, 1994, 1995; Johnson et al., 2015; Khairoutdinov & Emanuel, 2018; Kim et al., 2011, 2014, 2015; Lin & Mapes, 2004; Ma & Kuang, 2011; Raymond, 2001; Sobel & Gildor, 2003; Sobel et al., 2014; Zhang et al., 2019). From a quasi radiative-convective equilibrium perspective, enhanced tropical convective clouds reduce the outgoing long-wave radiation (OLR; $F_{TOA}$), resulting in a positive tendency of the column-integrated moist static energy (MSE; Neelin & Held, 1987). The recharge and discharge of MSE have been linked to the lifecycle of MJO (e.g., Bladé & Hartmann, 1993; Kemball-Cook & Weare, 2001). In addition to cloud longwave radiative forcing, the radiative forcing of the anomalous water vapor may also contribute to the column-integrated MSE tendency (Del Genio & Chen, 2015). Previous studies suggested that the MJO was associated with moisture anomalies whose vertical structures varied with convection strength and geographic location (e.g., Tian et al., 2006). The amplification and maintenance of MSE anomalies through radiative heating and surface fluxes destabilize the MJO disturbance (e.g., Inoue & Back, 2015; Kim et al., 2014; Sobel et al., 2014). However, modeling studies show different results concerning the role CRI plays in the MJO.

Hu and Randall (1994) reported the disappearance of intraseasonal oscillations in their single column model when the longwave cooling profile was fixed. Grabowski (2003) showed that CRI was not a necessary condition for a model using a cloud-resolving convection parameterization (or superparameterization) to produce MJO-like variability, although the CRI might enhance the convection-moisture feedback (Grabowski & Moncrieff, 2004). Enhancement of the convection-moisture feedback by CRI was present in a linear model used by Bony and Emanuel (2005). Bony and Emanuel (2005) also suggested that CRI reduces the phase

speed of large-scale tropical disturbances and slows down propagating waves. In another superparameterized general circulation model (GCM) study by Andersen and Kuang (2012), the authors showed that cloud longwave forcing is the dominant term in maintaining the MSE anomaly and retards its eastward propagation in the context of the MJO. In a cloud-permitting near-global equatorial aquaplanet model, the MJO-like disturbances become more like Kevin waves, if the longwave radiation is horizontally homogenized (Khairoutdinov & Emanuel, 2018). Using a conventional GCM, Maloney (2009) highlighted the role of the preconditioned moisture anomaly in the MJO and showed that horizontal advection and surface latent heat flux are the two leading terms in the column-integrated intraseasonal MSE budget. The enhanced surface latent heat flux is thought to be primarily driven by the enhanced surface wind (Maloney, 2009; Maloney & Sobel, 2004; Maloney et al., 2010).

An observational study in the Indian Ocean showed that moisture increases throughout the troposphere from 20 days before to 5 days after the MJO peak, although the relative humidity in the boundary layer is always above 80% during this period (DePasquale et al., 2014). In addition to moisture advection, the detrainment and evaporation of shallow cumulus and congestus are thought to contribute to the moisture preconditioning of the MJO (e.g., Johnson et al., 1999; Ruppert & Johnson, 2015). Based on a comparison of 20-year historical simulations from 24 climate models, Jiang et al. (2015) showed that an increased ratio of radiative cooling to latent heating tends to be associated with a decreased amplitude of intraseasonal variability in terms of daily rainfall anomalies during the boreal winter from the Indian Ocean to the West Pacific. One of the 24 models greatly improved MJO simulation (Jiang et al., 2015) by implementing a more realistic vertical structure of latent heating (Lappen & Schumacher, 2012). By analyzing the time-longitude rainfall pattern over the Indian Ocean, Jiang (2017) further suggests that the horizontal advection of MSE is a key process in MJO eastward propagation in both observations and simulations. MJO simulation is sensitive to moisture parameters in the model, such as entrainment rate and rain evaporation fraction (Hannah & Maloney, 2011). Although an increased entrainment rate may bring an improved hindcast of MJO precipitation and zonal wind, the improvement appears to result from erroneous compensation of overly high vertical MSE advection by overly low CRI (Hannah & Maloney, 2014). In other words, a model may improve performance of MJO simulations, even if the model physics is not close to observations.

Previous studies have shown that current GCMs have large differences in the fraction and water content of simulated clouds, particularly ice clouds (e.g., Jiang et al., 2012; Su et al., 2013; Tsushima et al., 2013; Vignesh et al., 2020; Wang & Su, 2013), which are believed to dominate the CRI in the context of MJO (e.g., Arnold & Randall, 2015; Zhang et al., 2019). Thus, a leading error source of diabatic heating in MJO simulations would be the uncertainties of simulated hydrometers that lead to the uncertainties of latent heating calculations and the input parameters to radiation schemes. In addition to the cloud properties, the behavior of the solutions to the atmospheric models is also sensitive to the selected radiation scheme, particularly the selected longwave radiation (i.e., terrestrial radiation) scheme (Wing et al., 2017). In a modeling study by Bretherton et al. (2005), the authors find that the midlevel inflow to the moist columns disappears when another radiation scheme is used, and they conclude that the convective mass flux is greatly responsive to radiative cooling perturbations. Hence, radiation scheme uncertainties may contribute to the differences among the modeling results obtained from the different studies summarized above. The dominant contribution to the radiative heating during the MJO wet phase is cloud longwave forcing, that is, reduced OLR (Lin & Mapes, 2004). In other words, the contribution from the cloud shortwave forcing is small (e.g., Andersen & Kuang, 2012; Lee et al., 2001). Many widely used fast radiation schemes do not include longwave cloud scattering effects, such as the Rapid Radiative Transfer Model (RRTM; Mlawer et al., 1997) and its simplified version for GCMs (RRTMG; Clough et al., 2005; Iacono et al., 2008). RRTMG has been used in global and regional models, including the Community Earth System Model (CESM; Kay et al., 2015) and Weather Research and Forecasting (WRF) model (Powers et al., 2017; Skamarock et al., 2008). Longwave scattering is ignored for two reasons: (1) Water vapor and cloud absorption contribute more significantly to radiation attenuation (i.e., extinction) than scattering in the longwave, and (2) the implementation of longwave scattering makes the radiation scheme more computationally costly (e.g., Chou et al., 1999). However, neglecting longwave scattering causes biases in estimated OLR and radiative heating.

Compared to the delta 128-stream reference model that includes longwave scattering, the absorption approximation method (no scattering) overestimates OLR by 1.9% (5.2 W m$^{-2}$), 2.7% (6.4 W m$^{-2}$), and 2.7% (6.0 W m$^{-2}$) in the presence of low, middle, and high clouds, respectively, in a midlatitude summer

atmosphere; corresponding OLR overestimations in a sub-Arctic winter atmosphere are 2.2% (4.4 W m$^{-2}$), 2.5% (4.8 W m$^{-2}$), and 2.5% (4.4 W m$^{-2}$) (Fu et al., 1997). Neglecting longwave scattering also underestimates the heating rate (*HR*) of the cloud layer, and the underestimation may reach more than 30% for an atmosphere containing high clouds (Fu et al., 1997). Chou et al. (1999) implemented longwave scattering into a radiation scheme using a scaling technique, and they reported a maximum *HR* relative error of ≈8% at the top and base of a cloud layer. Stephens et al. (2001) suggested that neglecting longwave scattering overestimates OLR by 8 W m$^{-2}$ in the global mean and locally up to 20 W m$^{-2}$. Based on field measurements of optically thin cirrus clouds, Joseph and Min (2003) suggest an OLR overestimation of 6–8 W m$^{-2}$ at most and *HR* errors of up to 0.2 K day$^{-1}$ if the longwave scattering is ignored.

By using cloud property data from the International Satellite Cloud Climatology Project (ISCCP) Version D2 (Rossow & Schiffer, 1991), Costa and Shine (2006) suggest an overestimation of OLR by 3.0 W m$^{-2}$ with longwave scattering ignored. Schmidt et al. (2006) suggest an overestimation of global mean OLR by 1.5 W m$^{-2}$ and an underestimation of global mean downward irradiance at the surface by 0.4 W m$^{-2}$ if the longwave scattering is neglected. Using 1 year of integrated A-Train observations, Kuo et al. (2017) suggest that longwave scattering of single-layer clouds decreases global annual mean OLR by 2.6 W m$^{-2}$ and increases surface downward irradiance by 1.2 W m$^{-2}$. Kuo et al. (2017) also show that longwave scattering increases *HR*s within and below cloud layers and the increased column-averaged *HR* is largest in the presence of high clouds.

Based on the results of the previous studies described above, it appears that neglecting longwave scattering underestimates column-integrated longwave heating and may underestimate the bottom or top heaviness of the radiative *HR* profile depending on the heights of the cloud layers. If the heating profile is bottom heavy, then the associated divergent circulation tends to recharge the column-integrated MSE; if the heating is top heavy, the associated circulation tends to discharge the column-integrated MSE (Kuang, 2011; Lappen & Schumacher, 2014; Ma & Kuang, 2011). Hence, we speculate that turning the longwave scattering on and off in a radiation scheme may lead to significantly different simulated behaviors of convection and intraseasonal variability over the tropics. However, to the best of our knowledge, none of the previous studies have evaluated the errors of OLR and *HR* introduced by neglecting longwave scattering by tropical clouds in the context of intraseasonal variability, such as the MJO, which is therefore the motivation of this study. The objective of this study is to examine the differences between longwave radiative cooling estimates with and without scattering calculations using satellite measurements of clouds from the Indian Ocean and Maritime Continent, where the MJO convective signal maximizes. The data and methods are introduced in section 2, followed by results in section 3. Conclusions are drawn in section 4.

## 2. Data and Methods

A recent study suggests that the CRI is strongest over the Indian Ocean and Maritime Continent (Zhang et al., 2019). Therefore, following the study by Del Genio and Chen (2015), we focus on cloud longwave radiation estimates over the equatorial Indian Ocean and Maritime Continent (5°N to 10°S, 65–170°E) in three longitudinal subsections (65–110°E, 110–130°E, and 130–170°E) that represent where the minimum OLR associated with deep convective clouds is present in MJO Phases 3, 5, and 6 during boreal winter (Wheeler & Hendon, 2004). We call the three subareas P3, P5, and P6 (Figure 1). The minimum OLR associated with Phase 4 spans the P3 and P5 regions, so we do not calculate statistics for that MJO phase. Boreal winter is the peak MJO season near the equator; in boreal summer, the main MJO convective activity shifts to north of the equator, including the Bay of Bengal and the South China Sea (e.g., Salby & Hendon, 1994; Zhang & Dong, 2004). We therefore focus on the 9 months outside of boreal summer (i.e., from September to May, hereafter referred to as the nonsummer months) over the study area, as in Del Genio and Chen (2015).

The A-Train integrated Cloud-Aerosol Lidar and Infrared Pathfinder Satellite Observation (CALIPSO), CloudSat, Clouds and the Earth's Radiant Energy System (CERES), and Moderate Resolution Imaging Spectroradiometer (MODIS) merged product Edition B1 (CCCM; Kato et al., 2010, 2011, 2014), which is a combination of spaceborne active and passive sensor measurements, has been used in several studies of cloud radiative effects (e.g., Gasparini et al., 2019; Hartmann & Berry, 2017; Kuo et al., 2017). In the CCCM data set, vertical profiles of cloud properties at a 333 m horizontal resolution from the
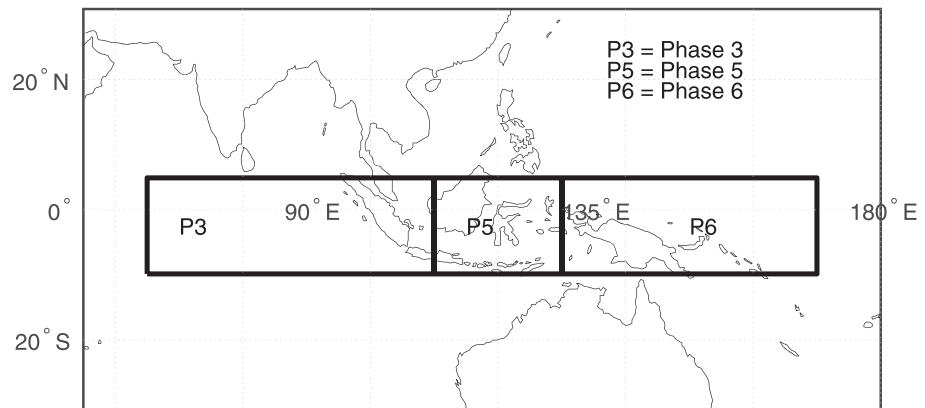
**Figure 1.** The study area. Each box represents the region where the minimum OLR occurs during a particular MJO phase.

Cloud-Aerosol Lidar with Orthogonal Polarization (CALIOP) on the CALIPSO satellite and at a 1.5 km horizontal resolution from the Cloud Profiling Radar (CPR) on the CloudSat satellite are first merged (averaged or interpolated) to the 1 km horizontal resolution of the MODIS pixels. CALIPSO is about 15 s behind CloudSat on average. The resultant 1 km cloud profiles are collocated with the CERES footprints. In each CERES footprint (about 20 km resolution), the 1 km atmospheric columns that have similar cloud top and base heights are grouped together (Kato et al., 2010). Based on the MODIS radiance measurements, the overall cloud optical properties of each cloud group—including cloud fraction, phase, visible optical thickness, and effective cloud particle size—are retrieved using the CERES cloud algorithm (Minnis et al., 2011). For the one-layer cloud groups, the cloud optical properties are derived using the so-called enhanced algorithm that also utilizes the collocated CALIOP and CPR cloud profiles (Kato et al., 2011). For the multilayer cloud groups, the optical properties of each cloud layer cannot be determined using the retrieved overall cloud optical properties unless additional assumptions are made. We therefore perform the longwave radiation calculations only for the one-layer cloud groups in the study area, as in Kuo et al. (2017). The mixed-phase deep convective clouds have large visible optical thickness and a cold cloud temperature and hence are regarded as one-layer ice clouds that have low cloud base heights in the CCCM data set. One caveat of the CCCM data set is that the retrieved cloud phase of the mixed-phase clouds—including the deep convective cores—is unrealistic, although the cloud top temperature and OLR should be close to reality. The statistics in section 3 are based on cloud properties first computed for each cloud group within CERES footprints and then area-averaged over P3, P5, and P6 for all A-Train overpasses in each day.

The CCCM data are available from July 2006 to April 2011, and the nonsummer months during September 2006 to May 2010 were selected for longwave radiation calculations. All of the MJO Phases 3, 5, and 6 periods were identified during these months using the Real-time Multivariate MJO (RMM) index (Wheeler & Hendon, 2004) for MJO events with RMM values >1. The first day of an MJO phase is called Day 0 in this study. The radiation flux and *HR* biases due to neglecting cloud longwave scattering were estimated for the one-layer cloud groups over the corresponding subareas in Figure 1 from 5 days before to 4 days after day 0 of every identified MJO phase period. It should be noted that there are multiple ways to define an MJO index (e.g., Liu et al., 2016; Maloney & Hartmann, 1998), although almost all indices capture the MJO leading modes in terms of low-level wind and precipitation. Because the MJO is strongest in the selected study area in December–February (DJF; Masunaga, 2007), the composite cloud properties and associated radiation fluxes for all identified MJO events were reported in DJF and other nonsummer months, respectively.

Using the longwave version of the RRTM (RRTM_LW; Mlawer et al., 1997), Tang et al. (2018) improved the scaling method by Chou et al. (1999) by adding an adjustment term to offset the top of the atmosphere (TOA) overestimation. Instead of assuming an isotropic blackbody ambient radiance distribution in the upper hemisphere when solving the upward radiance, Tang et al. (2018) use the downward radiance calculated

from the TOA to the surface as the ambient radiance in the upper hemisphere. The improved treatment of longwave scattering by Tang et al. (2018) is more accurate and approximately 20 times faster than the four-stream method. The RRTM_LW with the improved longwave scattering treatment by Tang et al. (2018) is adopted for radiation calculations in this study. The liquid cloud parameterization is taken from Kuo et al. (2017). Kuo et al. (2017) parameterized the single-scattering properties of cloud droplets for each of the 16 RRTM_LW bands from 10 to 3,250 $cm^{-1}$ based on the liquid cloud model used in Collection 6 of the MODIS cloud optical and microphysical products (Platnick et al., 2017). In this liquid cloud model, cloud droplets are assumed to be spheres and have a gamma size distribution with an effective variance of 0.1 (Platnick et al., 2017). Then, the Lorenz-Mie program (Bohren & Huffman, 2008) is used to calculate the single-scattering properties of the cloud droplets (Kuo et al., 2017) with the refractive index of water taken from Hale and Querry (1973) for wavelengths between 0.25 and 0.69 μm, Palmer and Williams (1974) for wavelengths between 0.69 and 2.0 μm, and Downing and Williams (1975) for wavelengths longer than 2.0 μm.

The ice cloud parameterizations are taken from Tang et al. (2018). Tang et al. (2018) parameterized the single-scattering properties of cloud ice particles for the RRTM_LW based on two recently developed ice particle models, the aggregate model and the two-habit model (THM). The aggregate model consists of surface-roughened eight-hexagonal-column aggregates (Yang et al., 2013) and is used in the MODIS Collection 6 cloud retrievals (Platnick et al., 2017). The THM consists of a mixture of surface-roughened single-hexagonal columns and 20-column aggregates (Loeb et al., 2018). The development of the THM was motivated by the observed increased complexity of ice particles with increasing particle size (Liu et al., 2014; Schmitt & Heymsfield, 2014). In agreement with the MODIS Collection 6 cloud retrievals (Platnick et al., 2017), a gamma size distribution with an effective variance of 0.1 is adopted here to derive the single-scattering properties of cloud ice particles (Tang et al., 2018). Loeb et al. (2018) suggest that broadband radiative flux calculations are sensitive to the selected ice particle model. Therefore, we use both the aggregate model and the THM in quantifying the radiation flux and *HR* biases introduced by neglecting longwave scattering.

Following the study by Kuo et al. (2017), the one-layer cloud is assumed to be homogenous in the radiation calculations. The cloud water path (CWP; g $m^{-2}$) is derived using the CCCM cloud optical depth ($\tau$) and effective radius ($r_{\text{eff}}$) retrievals (e.g., Grenfell & Warren, 1999; Stephens, 1978) with a density of water ($\rho_{\text{liquid}}$) of $10^6$ g $m^{-3}$ and a density of ice ($\rho_{\text{ice}}$) of $9.167 \times 10^5$ g $m^{-3}$ (e.g., Fu, 1996). The CCCM data also include the Goddard Earth Observing System (GEOS-5) Data Assimilation System reanalysis (Kato et al., 2014). The collocated GEOS-5 vertical profiles of pressure (hPa), temperature (K), water vapor mass mixing ratio (g $kg^{-1}$), and ozone mass mixing ratio (g $kg^{-1}$) are adopted in the radiation calculations in this study. Following Kuo et al. (2017), we let the volume mixing ratios of carbon dioxide ($CO_2$), nitrous oxide ($N_2O$), and methane ($CH_4$) take recent (year 2011) values of 390.5, 0.3242, and 1.803 ppmv, respectively, from the Fifth Assessment Report of the Intergovernmental Panel on Climate Change (Myhre et al., 2014). Because the surface types of the study areas shown in Figure 1 are mainly water and vegetation whose near-infrared emissivities are greater than 0.96 (Wilber et al., 1999), we set the surface emissivity to unity in our radiation calculations for simplicity. If a more realistic treatment of surface emissivity is implemented, the monthly mean OLR does not appear to change over the study areas in clear-sky and all-sky conditions (Huang et al., 2016). Tang et al. (2018) reported similar RRTM longwave radiation flux results if upward and downward radiances are calculated at two to four angles for the irradiance estimation. In this study, the radiances at four angles are chosen for the hemispheric integration in the radiation flux calculation.

The maximum and minimum longwave *HR*s are generally found at the cloud base and top, respectively, particularly for high clouds over the tropics (e.g., Ackerman et al., 1988; Dinh et al., 2010; Fu et al., 1997; Hartmann & Berry, 2017; Joseph & Min, 2003; Slingo & Slingo, 1988). If cloud longwave scattering is neglected, the largest *HR* errors are also present at the *HR* maximum and minimum (e.g., Fu et al., 1997; Joseph & Min, 2003). In addition, to quantify the radiation flux and *HR* biases, we also describe the corresponding cloud features. In each subarea (P3, P5, or P6 in Figure 1), we compute area-weighted averages of one-layer cloud area fractions, ice cloud area fractions of one-layer cloud groups, cloud top heights, and cloud base heights of all of the detected daytime and nighttime cloud groups in each day to obtain their daily mean values. The daily mean cloud feature sequences are averaged to get the pentad sequences for long-term
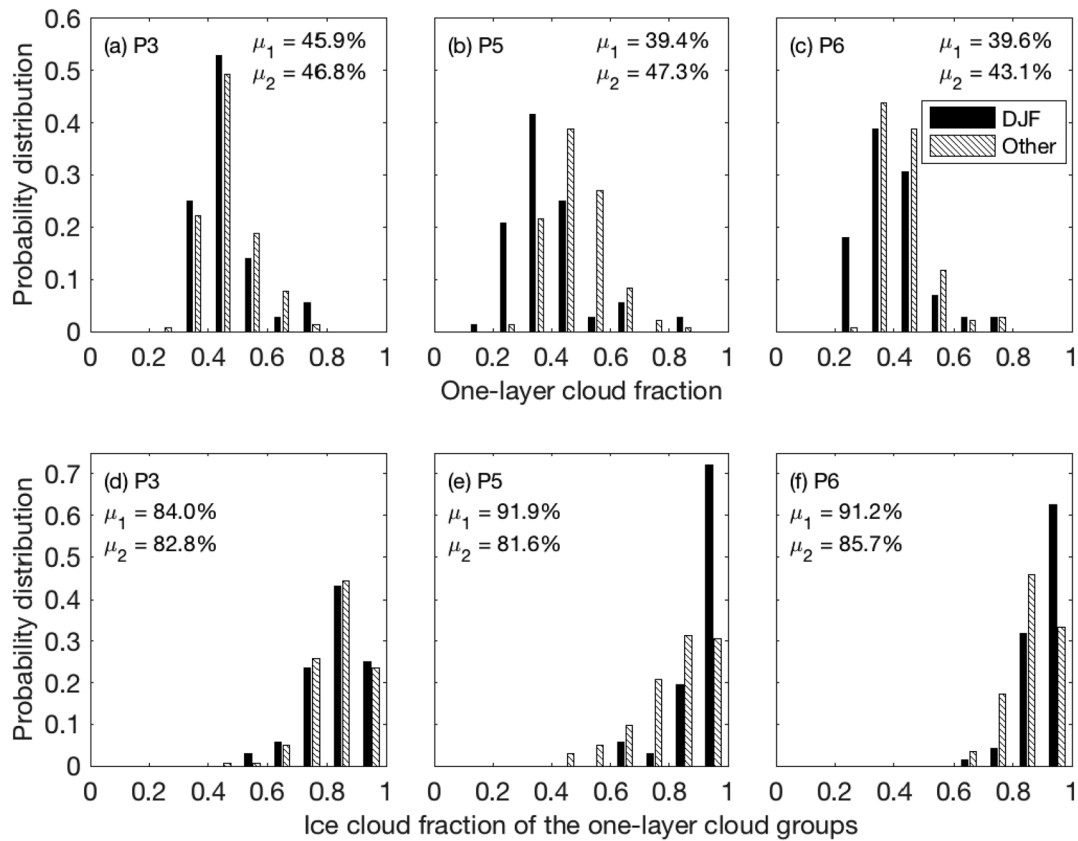
**Figure 2.** Probability distributions of the one-layer cloud area fraction (a–c) and ice cloud area fraction of the one-layer cloud groups (d–f) in DJF (black bars) and other nonsummer months (hatched bars) during September 2006 to May 2010 over the three study subareas: P3 (left panels), P5 (middle panels), and P6 (right panels). In the upper panels, $\mu_1$ and $\mu_2$ are the means of the pentad one-layer cloud fraction in DJF and other nonsummer months, respectively. In the lower panels, $\mu_1$ and $\mu_2$ are the means of the pentad ice cloud fraction of the one-layer cloud groups in DJF and other nonsummer months, respectively.

statistics. The daily mean cloud features are also used to derive their composite means and standard deviations during the 5 days before and 4 days after each MJO phase onset over the corresponding subarea. The same composite analysis is applied to $F_{TOA}$, net longwave radiation flux at the surface ($F_{SURF}$), the $HR$ profile, the $HR$ minimum at the cloud top height, and the $HR$ maximum at the cloud base height. As shown in the next section, the one-layer cloud groups consist primarily of ice clouds. We therefore focus on presenting the results for ice clouds and omit results about liquid clouds.

## 3. Results

### 3.1. One-Layer Cloud Groups

Kato et al. (2010) report that the CALIOP and CPR cloudy cases consist of about 50% each of one-layer and multilayer clouds. In Figure 2, the one-layer cloud groups account for 39–47% of the area of the CALIOP and CPR ground track in the nonsummer months during September 2006 to May 2010 (Figures 2a–2c). More than 80% of the detected one-layer cloud area is identified as ice cloud (Figures 2d–2f). Based on the $t$ test, the means of the one-layer area fraction is smaller in DJF than in other nonsummer months over subarea P5 ($p < 0.0001$), which has the largest percentage of continental area among the three subareas. The difference in the means of the one-layer area fraction between DJF and other nonsummer months is not significant over P3 and P6. The difference in the means of the ice cloud area fraction of the one-layer cloud groups between DJF and other nonsummer months is significant over P5 ($p < 0.0001$) and P6 ($p < 0.0001$), but not over P3.

Because many cirrus clouds in the tropics originate from anvil spreading out from deep convective clouds (e.g., Sassen et al., 2009), the increased one-layer ice cloud area fraction in DJF over P5 and P6 suggests the presence of more widespread deep convective clouds in this season. The peak convective activity in
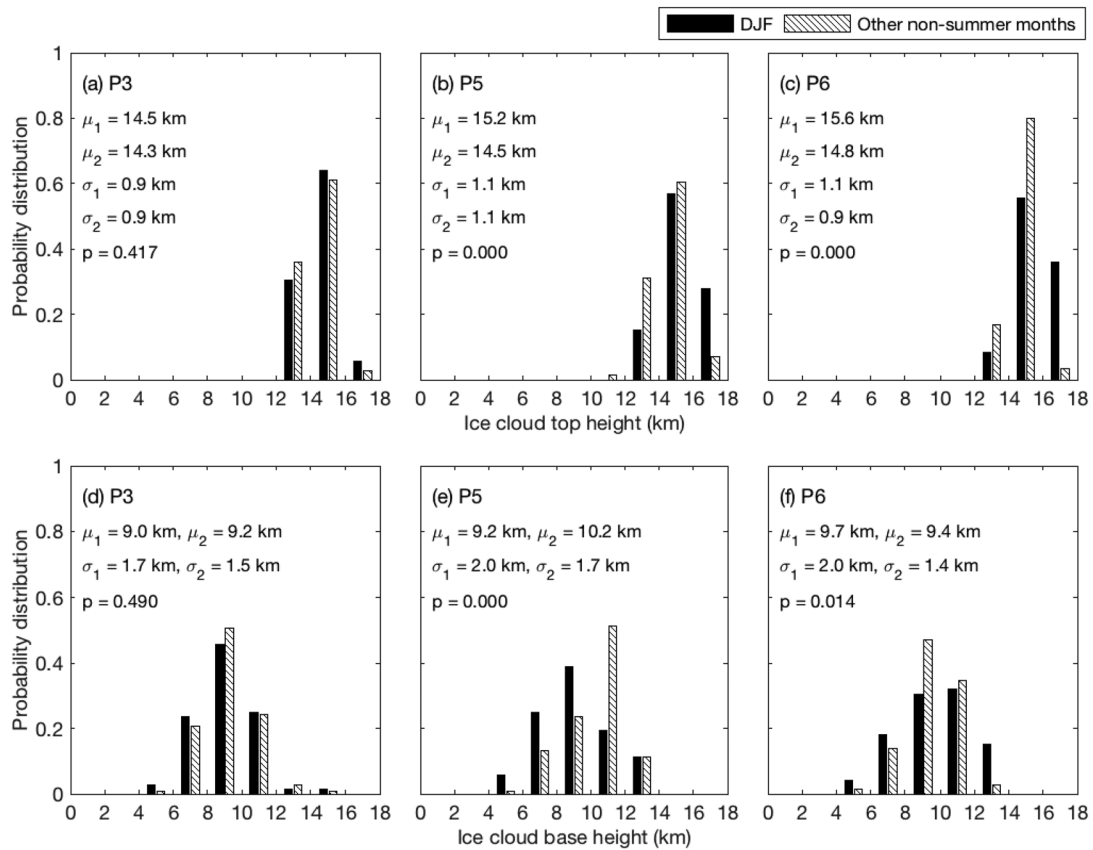
**Figure 3.** Probability distributions of the heights of the pentad one-layer ice cloud tops (a–c) and bases (d–f) in DJF (black bars) and other nonsummer months (hatched bars) during September 2006 to May 2010 over the three study subareas: P3 (a and d), P5 (b and e), and P6 (c and f). In all panels, $\mu_1$ and $\mu_2$ are the mean pentad heights, and $\sigma_1$ and $\sigma_2$ are the standard deviations in DJF and other nonsummer months, respectively. In each panel, $p$ is the $p$ value of the two-sided Kolmogorov-Smirnov test between the samples in DJF and other nonsummer months.

DJF over P5 and P6 is also evident in the higher ice cloud top heights in DJF (Figure 3), which are significantly higher than the other nonsummer months based on $t$ test results. The lower mean ice cloud base height in DJF over P5 is also significantly different compared to other months and may be due in part to the increased deep convection and associated thick anvil clouds that have not been detached from the deep convective cores (e.g., He et al., 2013; Massie et al., 2002). The mean ice cloud top and base heights over P3 do not show any statistically significant differences between DJF and the other nonsummer months, suggestive of only small seasonal variations of the parent deep convection over the Indian Ocean. Figure 3 also shows that convection is generally deeper over tropical continents (P5 and P6) than over tropical oceans (P3) because of the higher ice cloud top heights, which is a well-known feature (e.g., Liu et al., 2007; Williams & Stanfill, 2002).

### 3.2. Composite Cloud Fraction and Height

Based on the RMM index, there were 6 Phase 3 periods, 8 Phase 5 periods, and 10 Phase 6 periods in DJF and 9 Phase 3 periods, 15 Phase 5 periods, and 13 Phase 6 periods in other nonsummer months from September 2006 to May 2010. Table 1 documents the ranges of the composite mean one-layer cloud fraction from 5 days before to 4 days after the start day of each of the identified MJO phases. While the one-layer cloud fractions are similar in DJF and other nonsummer months over P3, the fraction in DJF is more than 10% smaller than that in other months over P5. The smallest composite means of one-layer cloud fraction over P3, P5, and P6 are present on Days −3, 0, and 1, respectively (Figure 4). The respective smallest means on Days 0 and 1 over P5 and P6 are presumably suggestive of a maximum overlap of

**Table 1**
*The Ranges of the Composite Mean One-Layer Cloud Fraction From 5 Days Before to 4 Days After the Start Day of Each of the Identified MJO Phases*

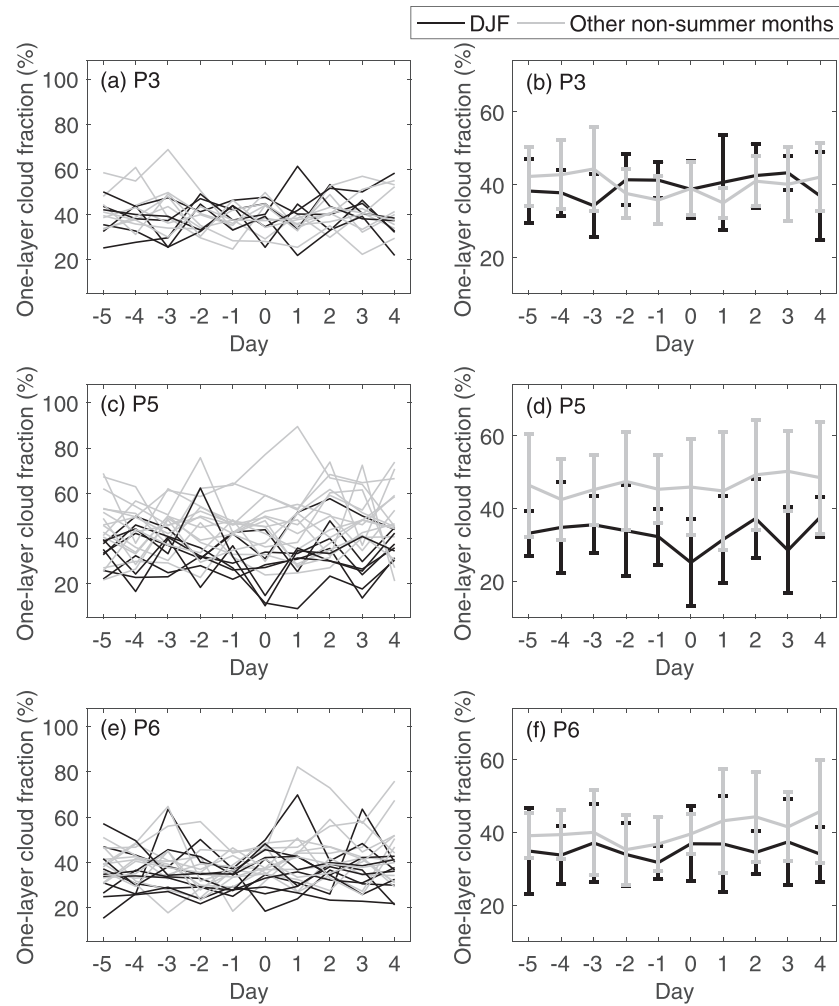| | P3 | | P5 | | P6 | |
|---|---|---|---|---|---|---|
| Fraction | DJF | Other | DJF | Other | DJF | Other |
| Lower bound | 34.2% | 35.0% | 25.2% | 42.5% | 31.7% | 35.2% |
| Upper bound | 43.3% | 44.3% | 37.7% | 50.2% | 37.4% | 45.8% |

**Figure 4.** One-layer cloud fractions from 5 days before to 4 days after the start day of each of the identified MJO phases in DJF (black) and other nonsummer months (gray) over the corresponding subarea. The left panels (a), (c), and (e) include the results for all the identified MJO phases over P3, P5, and P6, respectively; in the corresponding right panels (b), (d), and (f), the solid curves are the composite means, and the error bars are the standard deviations.

multiple strong detrainment layers that may be associated with the convection initiation of the MJO (Deng et al., 2016; Johnson et al., 1999). The largest composite means of one-layer cloud fraction over P3, P5, and P6 are present on Days 3, 4, and 3, respectively, presumably suggestive of a minimum overlap of the multiple strong detrainment layers when the MJO event is moving out of the associated subareas. The case-by-case variation of the one-layer cloud fraction is shown in the left panels of Figure 4. The greatest case-by-case variation over the P5 region may be due to the smaller sampling area and the larger land fraction over the this region than over the other two regions. Figure 5 shows that the area of one-layer cloud groups consists primarily of ice clouds from 5 days before to 4 days after the start day of each of the identified MJO phases. The case-by-case variation of the ice cloud fraction shown in the left panels of Figure 5 is greatest in the nonsummer months over P5, with much less variability during DJF and over the other subareas. Again, the strongest case-by-case variation over the P5 region may result from the smaller sampling area and the larger land portion over this region than over the other two selected regions. The composite means of the ice cloud fraction in the right panels of Figure 5 in DJF are above 88.0% over P3, above 91.0% over P5, and above 87.0% over P6; the means in other nonsummer months are above 85.0% over P3, above 73.0% over P5, and above 84.0% over P6. It also appears that the ice cloud fraction over each subarea before the MJO passage is significantly higher than the time-average mean. These results
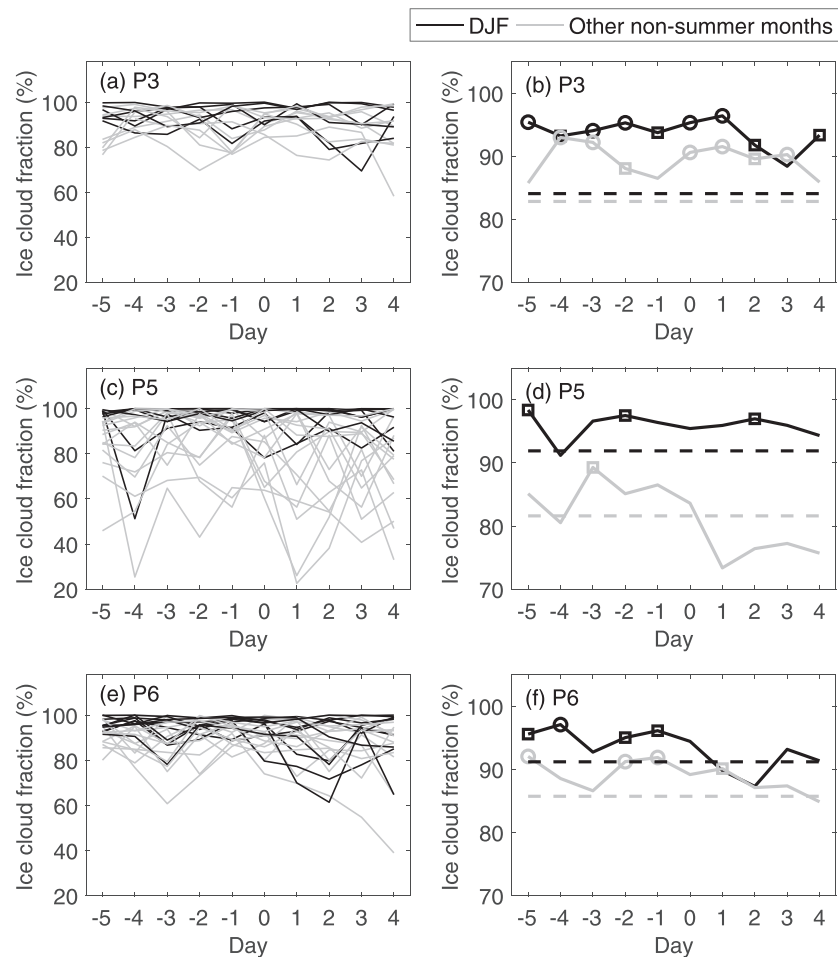
**Figure 5.** Ice cloud area fractions of one-layer cloud groups from 5 days before to 4 days after the start day of each of the identified MJO phases in DJF (black) and other nonsummer months (gray) over the corresponding subarea. The left panels (a), (c), and (e) include the results for all the identified MJO phases over P3, P5, and P6, respectively; in the corresponding right panels (b), (d), and (f), the solid curves are the composite means, and the dashed lines are the time-average means. The circles and squares in the right panel mark the composite means that are greater than the corresponding time-average means at significance levels of 0.01 and 0.05, respectively, based on a one-tail $t$ test. The daily mean ice cloud fraction data over each subarea was first averaged to get the pentad mean data, and the pentad mean data were then used for calculating the time-average mean and the significance test in DJF and other nonsummer months, respectively.

support a recent satellite study by Masunaga and Bony (2018), showing that heavy precipitating tropical convection is associated with increased cirrus clouds 1–2 days before, especially in moist atmospheres.

Masunaga and Bony (2018) hypothesize that the prevailing cirrus clouds before peak convection may be detrained from deep convective systems nearby and transported into the study area. Based on a trajectory analysis, Luo and Rossow (2004) find that detrained cirrus clouds have a lifetime of about $30 \pm 16$ hr and may travel a distance of about 1,000 km. A possible source of the convection could be from a previous MJO event. DePasquale et al. (2014) report the presence of significant nonprecipitating anvil and cirrus clouds after the rainfall cessation of the active MJO. Using the Tropical Rainfall Measuring Mission (TRMM) and two reanalysis data sets, Jiang et al. (2011) show that the radiative cooling minimum (or heating maximum) in the upper troposphere lags the MJO peak. The scattered isolated deep convection that occurs before an MJO active phase is thought to contribute to the increased preceding cirrus clouds as well (Masunaga & Bony, 2018).

Local cirrus formation is also a possible origin of the increased cirrus clouds before enhanced convection over the tropical oceans. Luo and Rossow (2004) show that more than half of the cirrus clouds (56%) over
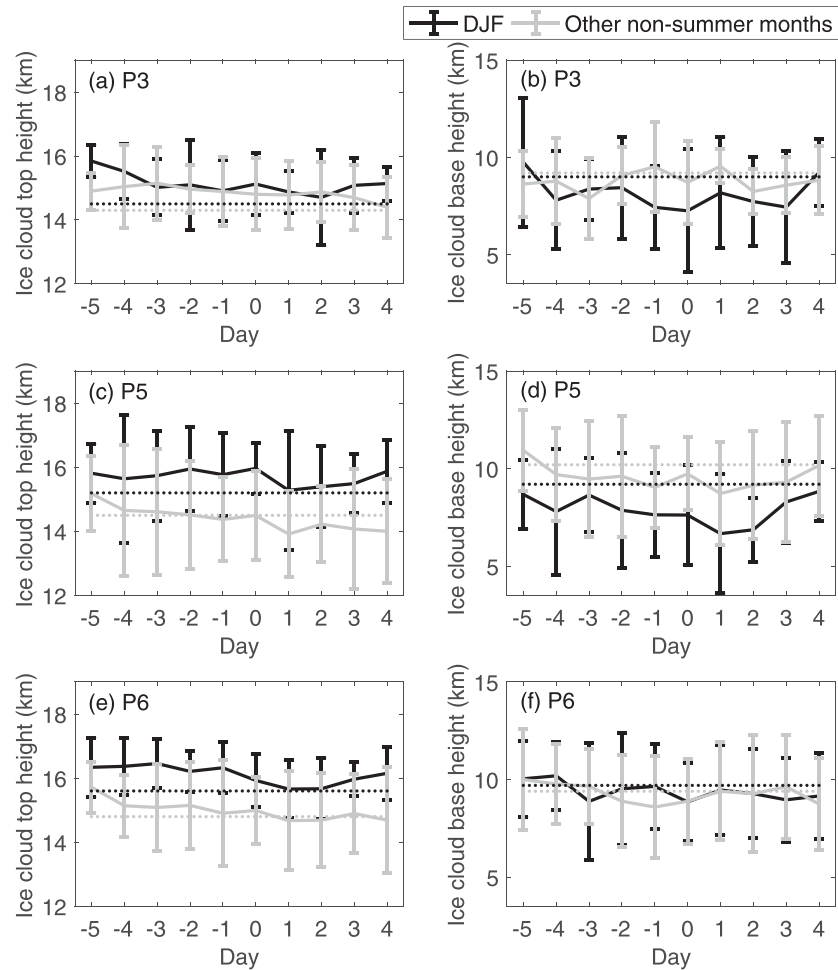
**Figure 6.** Composite mean one-layer ice cloud top (a, c, and e) and base (b, d, and f) heights from 5 days before to 4 days after the start day of all cases of the specified MJO phase in DJF (black) and other nonsummer months (gray) over the labeled subarea. The error bars mark the standard deviations. In each panel, the dotted lines are the corresponding time-average means shown in Figure 3.

the tropics are formed far away from deep convective cores, and hence, they attribute the formation of such cirrus to local transient upward air motions. Previous studies have shown that gravity waves can contribute to cirrus formation and cirrus property modulation (Barahona et al., 2017; Haag & Kärcher, 2004; Luo & Rossow, 2004; Prasad et al., 2019) through ice nucleation enhancement (Dinh et al., 2016; Jensen & Pfister, 2004; Jensen et al., 2009, 2016; Kim et al., 2016; Schoeberl et al., 2015; Ueyama et al., 2015), wave breaking (Homeyer et al., 2017), and reduced upper-tropospheric static stability (Trier & Sharman, 2016). Moreover, convectively coupled Kelvin waves may be present during different MJO stages (e.g., Gottschalck et al., 2013), and DePasquale et al. (2014) show that Kelvin wave passages during the MJO developing stage moisten the upper troposphere, which may in turn assist in situ cirrus production.

Figure 6 shows the time evolution of the one-layer ice cloud top and base heights for each subarea during the passage of the MJO. The seasonal mean averages from Figure 3 are indicated by the horizontal lines. It does not appear that the composite mean one-layer ice cloud heights are significantly different before and after the MJO passage, although there is a tendency for the ice cloud top height to decrease as the MJO evolves over each region, especially in DJF over P3 and in the other nonsummer months over P5 and P6. It is unclear if this decrease is from changes in the parent convection or from variations in the cirrus transport from other regions. Figure 6 also shows that the ice cloud tops are higher and bases are lower (except over P6) during DJF when the MJO is present over each region compared to the DJF mean values in Figure 3. Deep
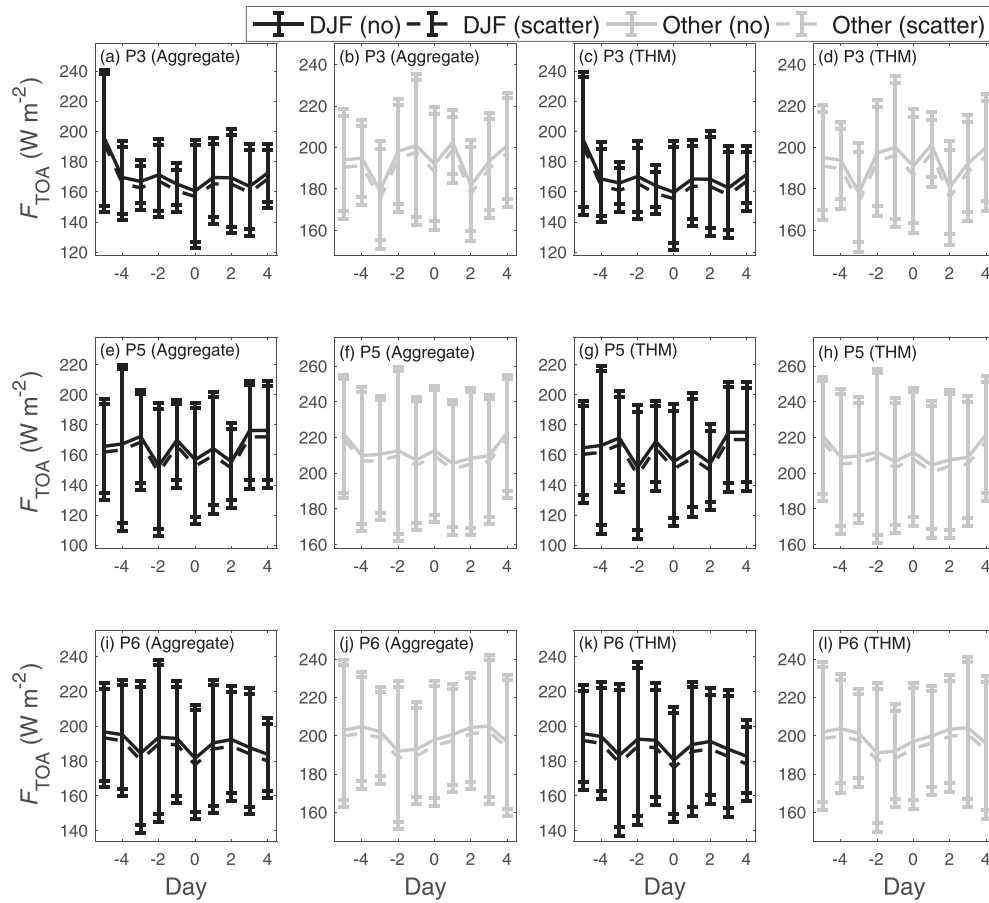
**Figure 7.** The composite net longwave radiation at the top of the atmosphere ($F_{TOA}$; W m$^{-2}$) from 5 days before to 4 days after the specified MJO phase onset in DJF (black) and other nonsummer months (gray) over the one-layer ice cloud area in P3, P5, and P6. In each panel, the solid lines are the composite $F_{TOA}$ means with longwave scattering ignored, and the dashed lines are the corresponding $F_{TOA}$ means with longwave scattering considered; the error bars mark the composite standard deviations. The first (a, e, and i) and second (b, f, and j) columns are based on the aggregate ice cloud particle model, and the third (c, g, and k) and fourth (d, h, and l) columns use the THM.

**Table 2**
*The Composite Mean $F_{TOA}$ Overestimation (W m$^{-2}$) Caused by Neglecting Longwave Scattering From 5 Days Before to 4 Days After the MJO Phase Onset (P3, P5, or P6) in DJF and Other Nonsummer Months Over the One-Layer Ice Cloud Portion of Subareas P3, P5, or P6*

| | P3 | | | | P5 | | | | P6 | | | |
| | Aggregate | | THM | | Aggregate | | THM | | Aggregate | | THM | |
| Day | DJF | Other | DJF | Other | DJF | Other | DJF | Other | DJF | Other | DJF | Other |
|---|---|---|---|---|---|---|---|---|---|---|---|---|
| −5 | 3.6 | 3.6 | 4.1 | 4.1 | 3.8 | 2.7 | 4.4 | 3.1 | 3.4 | 3.1 | 3.9 | 3.6 |
| −4 | 4.0 | 3.6 | 4.5 | 4.1 | 4.0 | 3.2 | 4.6 | 3.6 | 3.5 | 3.4 | 4.0 | 3.9 |
| −3 | 4.3 | 3.9 | 4.9 | 4.5 | 3.8 | 3.4 | 4.4 | 4.0 | 3.9 | 3.3 | 4.5 | 3.8 |
| −2 | 4.1 | 3.5 | 4.7 | 4.0 | 4.6 | 2.9 | 5.2 | 3.3 | 3.7 | 3.4 | 4.2 | 4.0 |
| −1 | 4.5 | 3.2 | 5.1 | 3.8 | 4.0 | 3.0 | 4.7 | 3.5 | 3.6 | 3.5 | 4.2 | 4.0 |
| 0 | 3.8 | 3.8 | 4.3 | 4.3 | 4.3 | 3.2 | 4.9 | 3.6 | 3.7 | 3.2 | 4.3 | 3.7 |
| 1 | 4.2 | 3.7 | 4.8 | 4.3 | 4.7 | 3.4 | 5.3 | 4.0 | 3.6 | 3.2 | 4.1 | 3.7 |
| 2 | 4.2 | 4.1 | 4.8 | 4.7 | 4.3 | 3.1 | 4.9 | 3.6 | 3.8 | 3.3 | 4.3 | 3.8 |
| 3 | 4.1 | 3.5 | 4.7 | 4.0 | 4.2 | 3.3 | 4.8 | 3.9 | 3.7 | 3.0 | 4.2 | 3.5 |
| 4 | 4.0 | 3.6 | 4.6 | 4.1 | 4.3 | 3.2 | 4.9 | 3.7 | 3.8 | 3.2 | 4.4 | 3.7 |
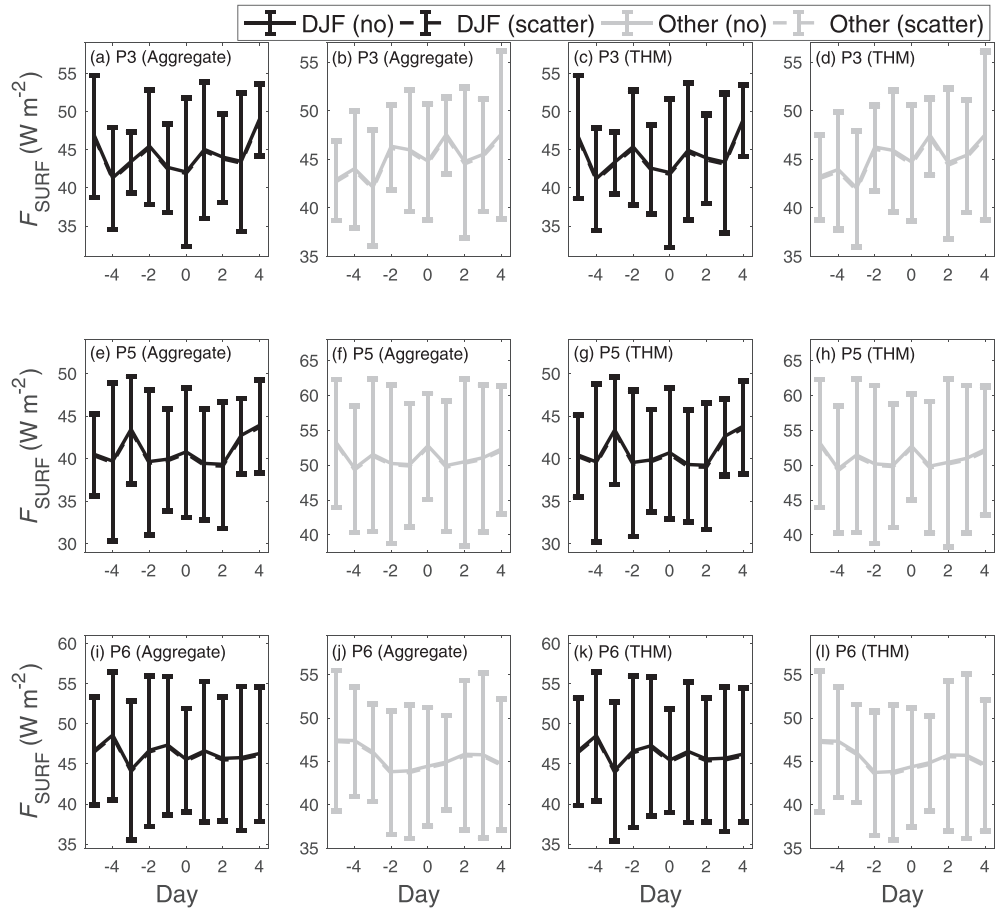
**Figure 8.** Same as Figure 7 except for $F_{SURF}$ (W m$^{-2}$).

convection is enhanced during the MJO, as is the stratiform rain associated with it (Lin et al., 2004). While deeper convection will increase the ice cloud top height, more robust stratiform rain production will lower the base of the anvil cloud. This change in DJF cloud heights agree with observed MJO seasonality (Masunaga, 2007; Salby & Hendon, 1994; Zhang & Dong, 2004).

### 3.3. Composite Radiation Flux

Figure 7 shows the composite means of $F_{TOA}$ with and without ice scattering over the one-layer ice cloud area from 5 days before to 4 days after the MJO onset in each region. The left panels assume an aggregate ice particle model, and the right panels assume a THM. The models are described in more detail in section 2. Using an aggregate ice particle model, the composite mean $F_{TOA}$ shows minimum values of 156.9 and 160.6 W m$^{-2}$ with and without scattering on Day 0 in DJF over P3. $F_{TOA}$ shows minimum values of 177.8 and 181.6 W m$^{-2}$ with and without scattering on Day 0 in DJF over P6. However, the $F_{TOA}$ minimum is present on Day $-2$ in DJF over P5 with values of 148.2 and 152.8 W m$^{-2}$ with and without scattering. If the THM is used, the minimum values of $F_{TOA}$ are 155.4 and 159.8 W m$^{-2}$ with and without scattering on Day 0 in DJF over P3 or 176.2 and 180.5 W m$^{-2}$ with and without scattering on Day 0 in DJF over P6, or 146.6 and 152.8 W m$^{-2}$ with and without scattering on Day $-2$ in DJF over P5. As shown in Figure 7, it does not appear that $F_{TOA}$ shows any obvious serial correlation in either DJF or other months.

The $F_{TOA}$ overestimations caused by neglecting longwave scattering over the one-layer ice cloud area are documented in Table 2, which shows that the $F_{TOA}$ overestimation does not have any obvious correlation with the time lead or lag from the passage of the MJO. In other words, the $F_{TOA}$ overestimation is a persistent bias during the MJO active phase. As documented in Table 2, the $F_{TOA}$ overestimation in DJF is around 3.5 to 5 W m$^{-2}$. If the cloud longwave scattering is neglected, the $F_{TOA}$ overestimation over the one-layer ice
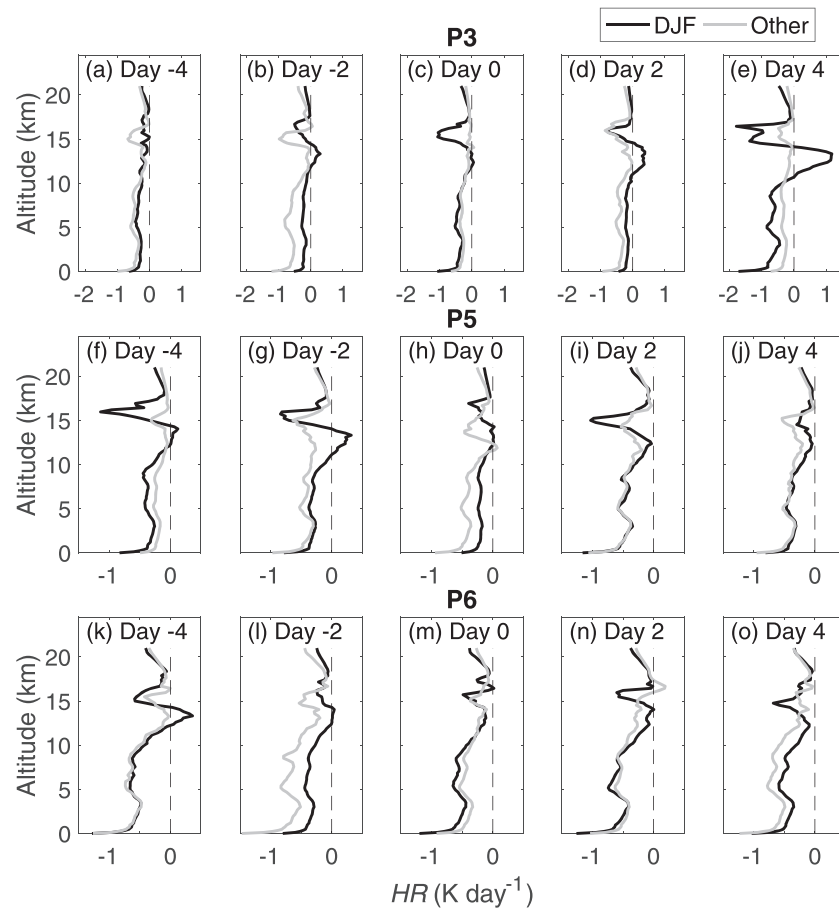
**Figure 9.** Composite mean area-weighted $HR$ calculations (K day$^{-1}$) with longwave scattering considered on days −4 (a, f, and k), −2 (b, g, and l), 0 (c, h, and m), 2 (d, i, and n), and 4 (e, j, and o) in DJF (black) and other nonsummer months (gray) over the one-layer ice cloudy area in the three subareas. The aggregate model is used in the calculations. P3 has a larger range in $x$-axis values.

cloud area based on the THM is about 0.5 W m$^{-2}$ larger than when using the aggregate model. One prominent feature of the THM is that the asymmetry factor decreases with increasing ice particle size (Loeb et al., 2018; Ren et al., 2020), meaning that THM assumes more backscattering, leading to a larger OLR overestimation. If cloud longwave scattering is included, the $F_{TOA}$ over the one-layer ice cloud area using the THM is about 1.5 W m$^{-2}$ smaller than when using the aggregate model.

If longwave cloud scattering is neglected, the $F_{SURF}$ overestimation underneath the one-layer ice cloud area is small and does not show large variations before and after the MJO phase onset (Figure 8). Both the aggregate model and THM suggest that the $F_{SURF}$ overestimation is limited to 0.2 to 0.3 W m$^{-2}$. Because the surface emissivity is set to unity in the radiation calculations, upward radiation flux estimations at the surface are determined by surface temperature only and not influenced by cloud longwave scattering. Consequently, the $F_{SURF}$ overestimation is completely accounted for by downward radiation flux underestimation at the surface. When cloud longwave scattering is considered, a part of the surface radiation emission will be scattered back to the surface by clouds.

The small $F_{SURF}$ bias over the study area in a nonscattering cloud atmosphere in the longwave is in agreement with previous studies (e.g., Kuo et al., 2017). Over the tropics, the ice clouds are high, and the atmosphere is humid (e.g., Slingo & Slingo, 1988). If cloud longwave scattering is considered over the tropics, part of the radiation emitted by the surface will be scattered back by clouds, but a large portion of the backscattered radiation will be absorbed by the water vapor below the clouds, and only a small portion can reach the surface. With higher clouds, more water vapor is below the clouds, and less backscattered radiation
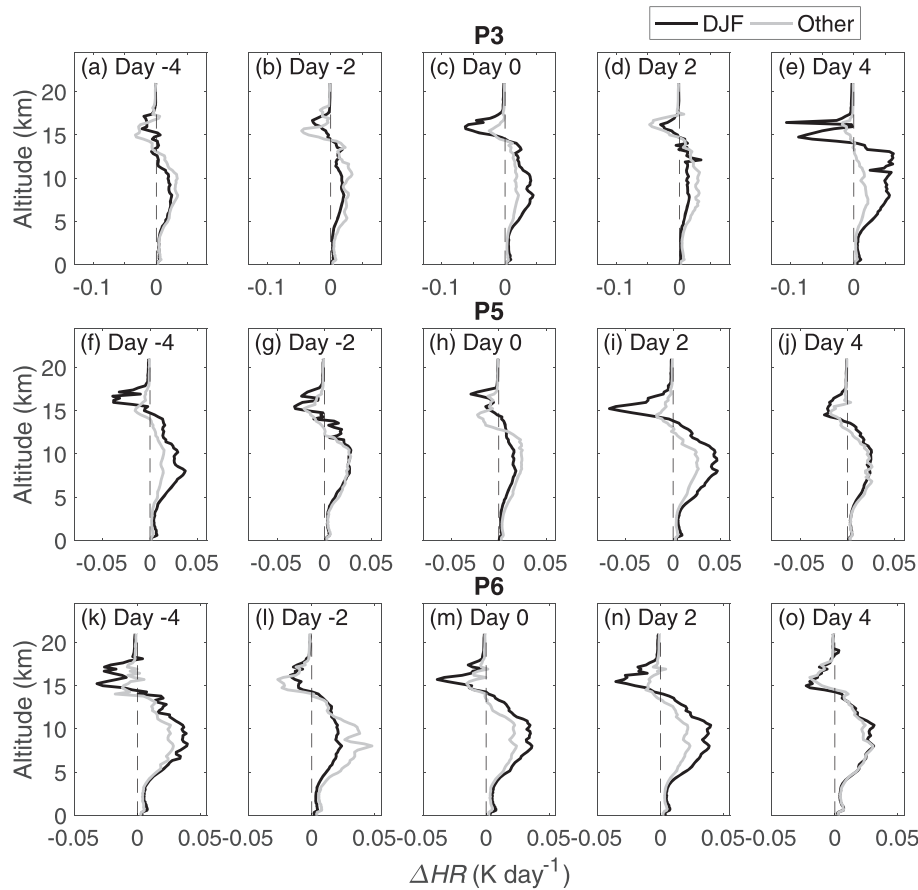
**Figure 10.** Same as Figure 9 except for the difference between *HR* calculations (*ΔHR*; K day$^{-1}$) with and without longwave scattering. P3 has a larger range in *x*-axis values.

reaches the surface. Consequently, the regional $F_{SURF}$ overestimation caused by neglecting longwave scattering is small over the one-layer ice cloud area in the Indian Ocean and Maritime Continent.

### 3.4. Composite *HR*

Figure 9 shows the time lag area-weighted *HR* profiles (K day$^{-1}$) for one-layer ice clouds with longwave scattering using the aggregate ice particle model. Using the THM leads to almost identical results. On most days, there is a peak in radiative cooling in the upper troposphere over each region and a sharp decrease in cooling (sometimes shifting to warming) below the peak, although there are variations in the resulting gradient based on day, region, and season. The gradient is strongest during DJF and at lag days farther away from Day 0 (e.g., Day 4 over P3 and Day −4 over P5 and P6). The gradient is generally weak on Day 0 over the three subregions, particularly in other nonsummer months, suggesting a stronger spatial variability of one-layer ice cloud top and base heights around the MJO convection initiation than before and after. Although individual homogenous cloud layer longwave *HR* can reach −60 K day$^{-1}$ at the cloud top and near 20 K day$^{-1}$ at the cloud base (e.g., Fu et al., 1997), the regional mean *HR* range shown in Figure 9 is bounded between −2.0 and 1.5 K day$^{-1}$. The small regional mean *HR* range is due to the cancelation of *HRs* of individual one-layer ice cloud groups, the top and base heights of which have a strong spatial variability.

Figure 10 shows the impact of including longwave scattering on the heating profiles from Figure 9. While the overall *ΔHR* values are

**Table 3**
*Composite Mean Maximum HR Overestimation (K day$^{-1}$) Range at Cloud Top Caused by Neglecting Longwave Scattering From 5 Days Before to 4 Days After the MJO Phase Onset in DJF and Other Nonsummer Months Over the One-Layer Ice Cloud Portion of the Corresponding Subarea*

| Subarea | Aggregate | | THM | |
|---|---|---|---|---|
| | DJF | Other | DJF | Other |
| P3 | 0.61 to 0.92 | 0.59 to 0.83 | 0.74 to 1.11 | 0.70 to 1.00 |
| P5 | 0.72 to 1.10 | 0.43 to 0.59 | 0.86 to 1.31 | 0.52 to 0.71 |
| P6 | 0.65 to 0.80 | 0.53 to 0.70 | 0.78 to 0.97 | 0.65 to 0.85 |

**Table 4**

*Composite Mean Maximum HR Underestimation (K day⁻¹) Range at Cloud Base Caused by Neglecting of Longwave Scattering From 5 Days Before to 4 Days After the MJO Phase Onset in DJF and Other Nonsummer Months Over the One-Layer Ice Cloud Portion of the Corresponding Subarea*

| | Aggregate | | THM | |
|---|---|---|---|---|
| Subarea | DJF | Other | DJF | Other |
| P3 | 0.47 to 0.72 | 0.42 to 0.52 | 0.56 to 0.84 | 0.50 to 0.64 |
| P5 | 0.37 to 0.74 | 0.34 to 0.52 | 0.44 to 0.87 | 0.42 to 0.63 |
| P6 | 0.42 to 0.53 | 0.39 to 0.55 | 0.50 to 0.64 | 0.47 to 0.66 |

small (<0.1 K day⁻¹), the change in the radiative heating profile is consistent across regions and seasons. There is a broad region of heating from around 5 km (i.e., the 0°C level in the tropics) up to 12–14 km representing highly varying cloud bases, consistent with the ice cloud base distributions in Figures 3d– 3f and the right column of Figure 6. There is a more narrow region of cooling near cloud top between 12 and 18 km, consistent with the ice cloud top height distributions in Figures 3a– 3c and the left column of Figure 6. This structure is similar to the observed longwave *HR*s in deep convective and cirrus regimes over Darwin and Manaus (Li et al., 2013). In addition, the magnitude of Δ*HR* tends to be larger in DJF, which has a higher one-layer ice cloud fraction (Figure 5), but does not appear to have a correlation with time during the evolution of the MJO.

At cloud-resolving scales, a sharper cloud base to cloud top heating gradient may sustain longer lasting anvil clouds (Hartmann et al., 2018) and hence enhance the MJO. The ranges of composite mean maximum *HR* overestimations and underestimations at the one-layer ice cloud top and base heights caused by neglecting longwave scattering are documented in Tables 3 and 4, respectively. The mean *HR* biases are around 1.0 K day⁻¹, more than an order magnitude greater than by averaging *HR* biases at the same height (Figure 10). As documented in Table 3, the composite mean *HR* overestimation at cloud top can reach 1.10 K day⁻¹ if the aggregate model is used; the overestimation can reach 1.31 K day⁻¹ if the THM is used. As documented in Table 4, the composite mean *HR* underestimation at cloud base can reach 0.74 K day⁻¹ with the aggregate model or 0.87 K day⁻¹ with the THM. The *HR* biases found in this study are close to the results reported by Fu et al. (1997) using a midlatitude summer high cloud case. If the cloud longwave scattering is included, the longwave radiation backscattered by the cloud layer is partly absorbed by the air at the cloud base, and hence, the reduction of the upward irradiance at the cloud top is greater than the increase of the downward irradiance at the cloud base. Because *HR* changes are proportional to the irradiance changes, the maximum *HR* overestimation due to neglecting longwave scattering at the cloud top is greater than the maximum *HR* underestimation at the cloud base.

## 4. Conclusions

Combined active and passive satellite cloud property retrievals are used to describe the one-layer cloud features from 5 days before to 4 days after the onset of MJO Phases 3, 5, and 6 in the boreal nonsummer months from the Indian Ocean to the Maritime Continent. The cloud property retrievals are also used to quantify the radiation calculation biases introduced by neglecting cloud longwave scattering using two different ice particle models. The results show that the satellite-detected one-layer cloud groups consist primarily of ice clouds, particularly during the MJO peak season of DJF. In addition, an increased ice cloud area fraction of one-layer cloud groups is present before the MJO passage, supporting a recent study that also finds the presence of increased cirrus clouds before heavily precipitating tropical convection (Masunaga & Bony, 2018). If longwave scattering is neglected, the composite mean OLR overestimation is approximately 3.5 to 5.0 W m⁻²; however, the overestimation of the net longwave radiation at the surface is small, only 0.2 to 0.3 W m⁻².

The composite mean *HR* overestimation at cloud top and underestimation at cloud base can reach 1.03 to 1.24 K day⁻¹ and 0.71 to 0.82 K day⁻¹, respectively, when cloud longwave scattering is neglected depending on whether an aggregate or two-habit ice particle model is used. Thus, if cloud longwave scattering is ignored, there is more heating at the cloud top and more cooling at the cloud base during the passage of the MJO, changing the heating profile gradient from cloud base to cloud top.

To briefly investigate the longwave scattering effects over the multilayer cloud regions, we carried out idealized radiation calculations for two thin ice cloud layers at 7–7.5 km and 11.5–12 km, respectively. If longwave scattering is included, the OLR reduction in the calculation with both cloud layers is close to that with only the upper cloud layer, but the *HR* increment at the cloud base and below has a maximum at a lower altitude in the two-layer cloud calculation than in the one-layer cloud calculation (not shown). Therefore, we suggest that the OLR overestimation due to neglecting cloud longwave scattering is similar

over the multilayer and one-layer ice cloud region but the *HR* underestimation underneath the cloud is largest at a lower altitude over the multilayer ice cloud regions than over the one-layer ice cloud regions.

Whether modeled MJO behavior is sensitive to this radiation calculation bias needs to be examined in future work. Based on the results presented in this study, we expect that the MJO-like disturbance will be stronger and its eastward propagation will be slower in superparameterized GCMs if cloud longwave scattering is included. In addition, previous studies have shown that cirrus clouds have a consistent diurnal pattern over the tropical continents (Sassen et al., 2009), and interactions between the diurnal variation of convection over the Maritime Continent and MJO have been reported (e.g., Birch et al., 2016; Fujita et al., 2011; Hagos et al., 2016; Ichikawa & Yasunari, 2008; Majda & Yang, 2016; Oh et al., 2012; Peatman et al., 2014; Rauniyar & Walsh, 2011; Sakaeda et al., 2017; Sui & Lau, 1992; Tung et al., 2014; Vincent & Lane, 2016, 2017; Zhang & Ling, 2017). Whether the radiation calculation biases introduced by neglecting longwave scattering have consistent diurnal variability is beyond the scope of this study and should be addressed in future studies.

## Data Availability Statement

The CCCM data set was acquired from the Atmosphere Science Data Center at the NASA Langley Research Center in Hampton, Virginia (https://eosweb.larc.nasa.gov/project/ceres/cer-news_cccm_aqua-fm3-modis-cal-cs_relb1_table/). The longwave version of the RRTM was acquired from the Atmospheric and Environmental Research (http://rtweb.aer.com/rrtm_frame.html). The RMM data were acquired from International Research Institute for Climate and Society/Lamont-Doherty Earth Observatory Climate Date Library at Columbia University (https://iridl.ldeo.columbia.edu/SOURCES/.BoM/.MJO/.RMM/).

## References

Ackerman, T. P., Liou, K.-N., Valero, F. P., & Pfister, L. (1988). Heating rates in tropical anvils. *Journal of the Atmospheric Sciences*, *45*(10), 1606–1623. https://doi.org/10.1175/1520-0469(1988)045%3C1606:HRITA%3E2.0.CO;2

Andersen, J. A., & Kuang, Z. (2012). Moist static energy budget of MJO-like disturbances in the atmosphere of a zonally symmetric aquaplanet. *Journal of Climate*, *25*(8), 2782–2804. https://doi.org/10.1175/JCLI-D-11-00168.1

Arnold, N. P., & Randall, D. A. (2015). Global-scale convective aggregation: Implications for the Madden-Julian Oscillation. *Journal of Advances in Modeling Earth Systems*, *7*, 1499–1518. https://doi.org/10.1002/2015MS000498

Barahona, D., Molod, A., & Kalesse, H. (2017). Direct estimation of the global distribution of vertical velocity within cirrus clouds. *Scientific Reports*, *7*(1), 6840. https://doi.org/10.1038/s41598-017-07038-6

Birch, C., Webster, S., Peatman, S., Parker, D., Matthews, A., Li, Y., & Hassim, M. (2016). Scale interactions between the MJO and the western Maritime Continent. *Journal of Climate*, *29*(7), 2471–2492. https://doi.org/10.1175/JCLI-D-15-0557.1

Bladé, I., & Hartmann, D. L. (1993). Tropical intraseasonal oscillations in a simple nonlinear model. *Journal of the Atmospheric Sciences*, *50*(17), 2922–2939. https://doi.org/10.1175/1520-0469(1993)050%3C2922:TIOIAS%3E2.0.CO;2

Bohren, C. F., & Huffman, D. R. (2008). *Absorption and scattering of light by small particles*. Weinheim, Germany: John Wiley & Sons.

Bony, S., & Emanuel, K. A. (2005). On the role of moist processes in tropical intraseasonal variability: Cloud-radiation and moisture-convection feedbacks. *Journal of the Atmospheric Sciences*, *62*(8), 2770–2789. https://doi.org/10.1175/JAS3506.1

Bretherton, C. S., Blossey, P. N., & Khairoutdinov, M. (2005). An energy-balance analysis of deep convective self-aggregation above uniform SST. *Journal of the Atmospheric Sciences*, *62*(12), 4273–4292. https://doi.org/10.1175/jas3614.1

Chou, M.-D., Lee, K.-T., Tsay, S.-C., & Fu, Q. (1999). Parameterization for cloud longwave scattering for use in atmospheric models. *Journal of Climate*, *12*(1), 159–169. https://doi.org/10.1175/1520-0442-12.1.159

Clough, S., Shephard, M., Mlawer, E., Delamere, J., Iacono, M., Cady-Pereira, K., et al. (2005). Atmospheric radiative transfer modeling: A summary of the AER codes. *Journal of Quantitative Spectroscopy and Radiative Transfer*, *91*(2), 233–244. https://doi.org/10.1016/j.jqsrt.2004.05.058

Costa, S., & Shine, K. (2006). An estimate of the global impact of multiple scattering by clouds on outgoing long-wave radiation. *Quarterly Journal of the Royal Meteorological Society*, *132*(616), 885–895. https://doi.org/10.1256/qj.05.169

Crueger, T., & Stevens, B. (2015). The effect of atmospheric radiative heating by clouds on the Madden-Julian Oscillation. *Journal of Advances in Modeling Earth Systems*, *7*, 854–864. https://doi.org/10.1002/2015MS000434

Del Genio, A. D., & Chen, Y. (2015). Cloud-radiative driving of the Madden-Julian Oscillation as seen by the A-Train. *Journal of Geophysical Research: Atmospheres*, *120*, 5344–5356. https://doi.org/10.1002/2015JD023278

Deng, M., Mace, G. G., & Wang, Z. (2016). Anvil productivities of tropical deep convective clusters and their regional differences. *Journal of the Atmospheric Sciences*, *73*(9), 3467–3487. https://doi.org/10.1175/JAS-D-15-0239.1

DePasquale, A., Schumacher, C., & Rapp, A. (2014). Radar observations of MJO and Kelvin wave interactions during DYNAMO/CINDY 2011/AMIE. *Journal of Geophysical Research: Atmospheres*, *119*, 6347–6367. https://doi.org/10.1002/2013JD021031

Dinh, T., Podglajen, A., Hertzog, A., Legras, B., & Plougonven, R. (2016). Effect of gravity wave temperature fluctuations on homogeneous ice nucleation in the tropical tropopause layer. *Atmospheric Chemistry and Physics*, *16*(1), 35–46. https://doi.org/10.5194/acp-16-35-2016

Dinh, T. P., Durran, D., & Ackerman, T. (2010). Maintenance of tropical tropopause layer cirrus. *Journal of Geophysical Research*, *115*, D02104. https://doi.org/10.1029/2009JD012735

Downing, H. D., & Williams, D. (1975). Optical constants of water in the infrared. *Journal of Geophysical Research*, *80*(12), 1656–1661. https://doi.org/10.1029/JC080i012p01656

Fu, Q. (1996). An accurate parameterization of the solar radiative properties of cirrus clouds for climate models. *Journal of Climate*, *9*(9), 2058–2082. https://doi.org/10.1175/1520-0442(1996)009%3C2058:AAPOTS%3E2.0.CO;2

Fu, Q., Liou, K., Cribb, M., Charlock, T., & Grossman, A. (1997). Multiple scattering parameterization in thermal infrared radiative transfer. *Journal of the Atmospheric Sciences*, *54*(24), 2799–2812. https://doi.org/10.1175/1520-0469(1997)054%3C2799:MSPITI%3E2.0.CO;2

Fujita, M., Yoneyama, K., Mori, S., Nasuno, T., & Satoh, M. (2011). Diurnal convection peaks over the eastern Indian Ocean off Sumatra during different MJO phases. *Journal of the Meteorological Society of Japan Series II*, *89*, 317–330. https://doi.org/10.2151/jmsj.2011-A22

Gasparini, B., Blossey, P. N., Hartmann, D. L., Lin, G., & Fan, J. (2019). What drives the life cycle of tropical anvil clouds? *Journal of Advances in Modeling Earth Systems*, *11*, 2586–2605. https://doi.org/10.1029/2019MS001736

Gottschalck, J., Roundy, P. E., Schreck, C. J. III, Vintzileos, A., & Zhang, C. (2013). Large-scale atmospheric and oceanic conditions during the 2011–12 DYNAMO field campaign. *Monthly Weather Review*, *141*(12), 4173–4196. https://doi.org/10.1175/MWR-D-13-00022.1

Grabowski, W. W. (2003). MJO-like coherent structures: Sensitivity simulations using the cloud-resolving convection parameterization (CRCP). *Journal of the Atmospheric Sciences*, *60*(6), 847–864. https://doi.org/10.1175/1520-0469(2003)060%3C0847:MLCSSS%3E2.0.CO;2

Grabowski, W. W., & Moncrieff, M. (2004). Moisture-convection feedback in the tropics. *Quarterly Journal of the Royal Meteorological Society*, *130*(604), 3081–3104. https://doi.org/10.1256/qj.03.135

Grenfell, T. C., & Warren, S. G. (1999). Representation of a nonspherical ice particle by a collection of independent spheres for scattering and absorption of radiation. *Journal of Geophysical Research*, *104*(D24), 31,697–31,709. https://doi.org/10.1029/1999JD900496

Haag, W., & Kärcher, B. (2004). The impact of aerosols and gravity waves on cirrus clouds at midlatitudes. *Journal of Geophysical Research*, *109*, D12202. https://doi.org/10.1029/2004JD004579

Hagos, S. M., Zhang, C., Feng, Z., Burleyson, C. D., De Mott, C., Kerns, B., et al. (2016). The impact of the diurnal cycle on the propagation of Madden-Julian Oscillation convection across the Maritime Continent. *Journal of Advances in Modeling Earth Systems*, *8*, 1552–1564. https://doi.org/10.1002/2016MS000725

Hale, G. M., & Querry, M. R. (1973). Optical constants of water in the 200-nm to 200-μm wavelength region. *Applied Optics*, *12*(3), 555–563. https://doi.org/10.1364/AO.12.000555

Hannah, W. M., & Maloney, E. D. (2011). The role of moisture-convection feedbacks in simulating the Madden–Julian oscillation. *Journal of Climate*, *24*(11), 2754–2770. https://doi.org/10.1175/2011JCLI3803.1

Hannah, W. M., & Maloney, E. D. (2014). The moist static energy budget in NCAR CAM5 hindcasts during DYNAMO. *Journal of Advances in Modeling Earth Systems*, *6*, 420–440. https://doi.org/10.1002/2013MS000272

Hartmann, D. L., & Berry, S. E. (2017). The balanced radiative effect of tropical anvil clouds. *Journal of Geophysical Research: Atmospheres*, *122*, 5003–5020. https://doi.org/10.1002/2017JD026460

Hartmann, D. L., Gasparini, B., Berry, S. E., & Blossey, P. N. (2018). The life cycle and net radiative effect of tropical anvil clouds. *Journal of Advances in Modeling Earth Systems*, *10*, 3012–3029. https://doi.org/10.1029/2018MS001484

He, Q., Li, C., Ma, J., Wang, H., Shi, G., Liang, Z., et al. (2013). The properties and formation of cirrus clouds over the Tibetan Plateau based on summertime lidar measurements. *Journal of the Atmospheric Sciences*, *70*(3), 901–915. https://doi.org/10.1175/JAS-D-12-0171.1

Homeyer, C. R., McAuliffe, J. D., & Bedka, K. M. (2017). On the development of above-anvil cirrus plumes in extratropical convection. *Journal of the Atmospheric Sciences*, *74*(5), 1617–1633. https://doi.org/10.1175/JAS-D-16-0269.1

Hu, Q., & Randall, D. A. (1994). Low-frequency oscillations in radiative-convective systems. *Journal of the Atmospheric Sciences*, *51*(8), 1089–1099. https://doi.org/10.1175/1520-0469(1994)051%3C1089:LFOIRC%3E2.0.CO;2

Hu, Q., & Randall, D. A. (1995). Low-frequency oscillations in radiative-convective systems. Part II: An idealized model. *Journal of the Atmospheric Sciences*, *52*(4), 478–490. https://doi.org/10.1175/1520-0469(1995)052%3C0478:LFOIRC%3E2.0.CO;2

Huang, X., Chen, X., Zhou, D. K., & Liu, X. (2016). An observationally based global band-by-band surface emissivity dataset for climate and weather simulations. *Journal of the Atmospheric Sciences*, *73*(9), 3541–3555. https://doi.org/10.1175/JAS-D-15-0355.1

Iacono, M. J., Delamere, J. S., Mlawer, E. J., Shephard, M. W., Clough, S. A., & Collins, W. D. (2008). Radiative forcing by long-lived greenhouse gases: Calculations with the AER radiative transfer models. *Journal of Geophysical Research*, *113*, D13103. https://doi.org/10.1029/2008JD009944

Ichikawa, H., & Yasunari, T. (2008). Intraseasonal variability in diurnal rainfall over New Guinea and the surrounding oceans during austral summer. *Journal of Climate*, *21*(12), 2852–2868. https://doi.org/10.1175/2007JCLI1784.1

Inoue, K., & Back, L. (2015). Column-integrated moist static energy budget analysis on various time scales during TOGA COARE. *Journal of the Atmospheric Sciences*, *72*(5), 1856–1871. https://doi.org/10.1175/JAS-D-14-0249.1

Jensen, E., Lawson, P., Baker, B., Pilson, B., Mo, Q., Heymsfield, A., et al. (2009). On the importance of small ice crystals in tropical anvil cirrus. *Atmospheric Chemistry and Physics*, *9*(15), 5519–5537. https://doi.org/10.5194/acp-9-5519-2009

Jensen, E., & Pfister, L. (2004). Transport and freeze-drying in the tropical tropopause layer. *Journal of Geophysical Research*, *109*, D02207. https://doi.org/10.1029/2003JD004022

Jensen, E. J., Ueyama, R., Pfister, L., Bui, T. V., Alexander, M. J., Podglajen, A., et al. (2016). High-frequency gravity waves and homogeneous ice nucleation in tropical tropopause layer cirrus. *Geophysical Research Letters*, *43*, 6629–6635. https://doi.org/10.1002/2016GL069426

Jiang, J. H., Su, H., Zhai, C., Perun, V. S., Del Genio, A., Nazarenko, L. S., et al. (2012). Evaluation of cloud and water vapor simulations in CMIP5 climate models using NASA "A-Train" satellite observations. *Journal of Geophysical Research*, *117*, D14105. https://doi.org/10.1029/2011JD017237

Jiang, X. (2017). Key processes for the eastward propagation of the Madden-Julian Oscillation based on multimodel simulations. *Journal of Geophysical Research: Atmospheres*, *122*, 755–770. https://doi.org/10.1002/2016JD025955

Jiang, X., Waliser, D. E., Olson, W. S., Tao, W.-K., L'Ecuyer, T. S., Li, K.-F., et al. (2011). Vertical diabatic heating structure of the MJO: Intercomparison between recent reanalyses and TRMM estimates. *Monthly Weather Review*, *139*(10), 3208–3223. https://doi.org/10.1175/2011MWR3636.1

Jiang, X., Waliser, D. E., Xavier, P. K., Petch, J., Klingaman, N. P., Woolnough, S. J., et al. (2015). Vertical structure and physical processes of the Madden-Julian Oscillation: Exploring key model physics in climate simulations. *Journal of Geophysical Research: Atmospheres*, *120*, 4718–4748. https://doi.org/10.1002/2014JD022375

Johnson, R. H., Ciesielski, P. E., Ruppert, J. H. Jr., & Katsumata, M. (2015). Sounding-based thermodynamic budgets for DYNAMO. *Journal of the Atmospheric Sciences*, *72*(2), 598–622. https://doi.org/10.1175/JAS-D-14-0202.1

Johnson, R. H., Rickenbach, T. M., Rutledge, S. A., Ciesielski, P. E., & Schubert, W. H. (1999). Trimodal characteristics of tropical convection. *Journal of Climate*, *12*(8), 2397–2418. https://doi.org/10.1175/1520-0442(1999)012%3C2397:TCOTC%3E2.0.CO;2

Joseph, E., & Min, Q. (2003). Assessment of multiple scattering and horizontal inhomogeneity in IR radiative transfer calculations of observed thin cirrus clouds. *Journal of Geophysical Research*, *108*(D13), 4380. https://doi.org/10.1029/2002JD002831

Kato, S., Miller, W. F., Sun-Mack, S., Rose, F. G., Chen, Y., & Mlynczak, P. E. (2014). Variable descriptions of the A-Train integrated CALIPSO. CloudSat, CERES, and MODIS merged product (CCCM or C3M)*, NEWS A-Train variable descriptions*.

Kato, S., Rose, F. G., Sun-Mack, S., Miller, W. F., Chen, Y., Rutan, D. A., et al. (2011). Improvements of top-of-atmosphere and surface irradiance computations with CALIPSO-, CloudSat-, and MODIS-derived cloud and aerosol properties. *Journal of Geophysical Research*, *116*, D19209. https://doi.org/10.1029/2011JD016050

Kato, S., Sun-Mack, S., Miller, W. F., Rose, F. G., Chen, Y., Minnis, P., & Wielicki, B. A. (2010). Relationships among cloud occurrence frequency, overlap, and effective thickness derived from CALIPSO and CloudSat merged cloud vertical profiles. *Journal of Geophysical Research*, *115*, D00H28. https://doi.org/10.1029/2009JD012277

Kay, J., Deser, C., Phillips, A., Mai, A., Hannay, C., Strand, G., et al. (2015). The Community Earth System Model (CESM) large ensemble project: A community resource for studying climate change in the presence of internal climate variability. *Bulletin of the American Meteorological Society*, *96*(8), 1333–1349. https://doi.org/10.1175/BAMS-D-13-00255.1

Kemball-Cook, S. R., & Weare, B. C. (2001). The onset of convection in the Madden-Julian Oscillation. *Journal of Climate*, *14*(5), 780–793. https://doi.org/10.1175/1520-0442(2001)014%3C0780:TOOCIT%3E2.0.CO;2

Khairoutdinov, M. F., & Emanuel, K. (2018). Intraseasonal variability in a cloud-permitting near-global equatorial aquaplanet model. *Journal of the Atmospheric Sciences*, *75*(12), 4337–4355. https://doi.org/10.1175/JAS-D-18-0152.1

Kim, D., Ahn, M.-S., Kang, I.-S., & Del Genio, A. D. (2015). Role of longwave cloud-radiation feedback in the simulation of the Madden-Julian oscillation. *Journal of Climate*, *28*(17), 6979–6994. https://doi.org/10.1175/JCLI-D-14-00767.1

Kim, D., Kug, J.-S., & Sobel, A. H. (2014). Propagating versus nonpropagating Madden-Julian Oscillation events. *Journal of Climate*, *27*(1), 111–125. https://doi.org/10.1175/JCLI-D-13-00084.1

Kim, D., Sobel, A. H., & Kang, I. S. (2011). A mechanism denial study on the Madden-Julian Oscillation. *Journal of Advances in Modeling Earth Systems*, *3*, M12007. https://doi.org/10.1029/2011MS000081

Kim, J. E., Alexander, M. J., Bui, T. P., Dean-Day, J. M., Lawson, R. P., Woods, S., et al. (2016). Ubiquitous influence of waves on tropical high cirrus clouds. *Geophysical Research Letters*, *43*, 5895–5901. https://doi.org/10.1002/2016GL069293

Kuang, Z. (2011). The wavelength dependence of the gross moist stability and the scale selection in the instability of column-integrated moist static energy. *Journal of the Atmospheric Sciences*, *68*(1), 61–74. https://doi.org/10.1175/2010JAS3591.1

Kuo, C. P., Yang, P., Huang, X., Feldman, D., Flanner, M., Kuo, C., & Mlawer, E. J. (2017). Impact of multiple scattering on longwave radiative transfer involving clouds. *Journal of Advances in Modeling Earth Systems*, *9*, 3082–3098. https://doi.org/10.1002/2017MS001117

Lappen, C. L., & Schumacher, C. (2014). The role of tilted heating in the evolution of the MJO. *Journal of Geophysical Research: Atmospheres*, *119*, 2966–2989. https://doi.org/10.1002/2013JD020638

Lappen, C.-L., & Schumacher, C. (2012). Heating in the tropical atmosphere: What level of detail is critical for accurate MJO simulations in GCMs? *Climate Dynamics*, *39*(9–10), 2547–2568. https://doi.org/10.1007/s00382-012-1327-y

Lee, M. I., Kang, I. S., Kim, J. K., & Mapes, B. E. (2001). Influence of cloud-radiation interaction on simulating tropical intraseasonal oscillation with an atmospheric general circulation model. *Journal of Geophysical Research*, *106*(D13), 14,219–14,233. https://doi.org/10.1029/2001JD900143

Li, W., Schumacher, C., & McFarlane, S. A. (2013). Radiative heating of the ISCCP upper level cloud regimes and its impact on the large-scale tropical circulation. *Journal of Geophysical Research: Atmospheres*, *118*, 592–604. https://doi.org/10.1002/jgrd.50114

Lin, J., Mapes, B., Zhang, M., & Newman, M. (2004). Stratiform precipitation, vertical heating profiles, and the Madden-Julian oscillation. *Journal of the Atmospheric Sciences*, *61*(3), 296–309. https://doi.org/10.1175/1520-0469(2004)061%3C0296:SPVHPA%3E2.0.CO;2

Lin, J.-L., & Mapes, B. E. (2004). Radiation budget of the tropical intraseasonal oscillation. *Journal of the Atmospheric Sciences*, *61*(16), 2050–2062. https://doi.org/10.1175/1520-0469(2004)061%3C2050:RBOTTI%3E2.0.CO;2

Liu, C., Yang, P., Minnis, P., Loeb, N., Kato, S., Heymsfield, A., & Schmitt, C. (2014). A two-habit model for the microphysical and optical properties of ice clouds. *Atmospheric Chemistry and Physics*, *14*(24), 13,719–13,737. https://doi.org/10.5194/acp-14-13719-2014

Liu, C. T., Zipser, E. J., & Nesbitt, S. W. (2007). Global distribution of tropical deep convection: Different perspectives from TRMM infrared and radar data. *Journal of Climate*, *20*(3), 489–503. https://doi.org/10.1175/jcli4023.1

Liu, P., Zhang, Q., Zhang, C., Zhu, Y., Khairoutdinov, M., Kim, H.-M., et al. (2016). A revised real-time multivariate MJO index. *Monthly Weather Review*, *144*(2), 627–642. https://doi.org/10.1175/MWR-D-15-0237.1

Loeb, N. G., Yang, P., Rose, F. G., Hong, G., Sun-Mack, S., Minnis, P., et al. (2018). Impact of ice cloud microphysics on satellite cloud retrievals and broadband flux radiative transfer model calculations. *Journal of Climate*, *31*(5), 1851–1864. https://doi.org/10.1175/JCLI-D-17-0426.1

Luo, Z., & Rossow, W. B. (2004). Characterizing tropical cirrus life cycle, evolution, and interaction with upper-tropospheric water vapor using Lagrangian trajectory analysis of satellite observations. *Journal of Climate*, *17*(23), 4541–4563. https://doi.org/10.1175/3222.1

Ma, D., & Kuang, Z. (2011). Modulation of radiative heating by the Madden-Julian Oscillation and convectively coupled Kelvin waves as observed by CloudSat. *Geophysical Research Letters*, *38*, L21813. https://doi.org/10.1029/2011GL049734

Madden, R. A., & Julian, P. R. (1971). Detection of a 40–50 day oscillation in the zonal wind in the tropical Pacific. *Journal of the Atmospheric Sciences*, *28*(5), 702–708. https://doi.org/10.1175/1520-0469(1971)028%3C0702:DOADOI%3E2.0.CO;2

Madden, R. A., & Julian, P. R. (1972). Description of global-scale circulation cells in the tropics with a 40–50 day period. *Journal of the Atmospheric Sciences*, *29*(6), 1109–1123. https://doi.org/10.1175/1520-0469(1972)029%3C1109:DOGSCC%3E2.0.CO;2

Majda, A. J., & Yang, Q. (2016). A multiscale model for the intraseasonal impact of the diurnal cycle over the Maritime Continent on the Madden-Julian oscillation. *Journal of the Atmospheric Sciences*, *73*(2), 579–604. https://doi.org/10.1175/JAS-D-15-0158.1

Maloney, E. D. (2009). The moist static energy budget of a composite tropical intraseasonal oscillation in a climate model. *Journal of Climate*, *22*(3), 711–729. https://doi.org/10.1175/2008JCLI2542.1

Maloney, E. D., & Hartmann, D. L. (1998). Frictional moisture convergence in a composite life cycle of the Madden-Julian oscillation. *Journal of Climate*, *11*(9), 2387–2403. https://doi.org/10.1175/1520-0442(1998)011%3C2387:FMCIAC%3E2.0.CO;2

Maloney, E. D., & Sobel, A. H. (2004). Surface fluxes and ocean coupling in the tropical intraseasonal oscillation. *Journal of Climate*, *17*(22), 4368–4386. https://doi.org/10.1175/JCLI-3212.1

Maloney, E. D., Sobel, A. H., & Hannah, W. M. (2010). Intraseasonal variability in an aquaplanet general circulation model. *Journal of Advances in Modeling Earth Systems*, *2*, 5. https://doi.org/10.3894/JAMES.2010.2.5

Massie, S., Gettelman, A., Randel, W., & Baumgardner, D. (2002). Distribution of tropical cirrus in relation to convection. *Journal of Geophysical Research*, *107*(D21), 4591. https://doi.org/10.1029/2001JD001293

Masunaga, H. (2007). Seasonality and regionality of the Madden-Julian oscillation, Kelvin wave, and equatorial Rossby wave. *Journal of the Atmospheric Sciences*, *64*(12), 4400–4416. https://doi.org/10.1175/2007JAS2179.1

Masunaga, H., & Bony, S. (2018). Radiative invigoration of tropical convection by preceding cirrus clouds. *Journal of the Atmospheric Sciences*, *75*(4), 1327–1342. https://doi.org/10.1175/JAS-D-17-0355.1

Minnis, P., Sun-Mack, S., Young, D. F., Heck, P. W., Garber, D. P., Chen, Y., et al. (2011). CERES Edition-2 cloud property retrievals using TRMM VIRS and Terra and Aqua MODIS data—Part I: Algorithms. *IEEE Transactions on Geoscience and Remote Sensing*, *49*(11), 4374–4400. https://doi.org/10.1109/TGRS.2011.2144601

Mlawer, E. J., Taubman, S. J., Brown, P. D., Iacono, M. J., & Clough, S. A. (1997). Radiative transfer for inhomogeneous atmospheres: RRTM, a validated correlated-k model for the longwave. *Journal of Geophysical Research*, *102*(D14), 16,663–16,682. https://doi.org/10.1029/97JD00237

Myhre, G., Shindell, D., & Pongratz, J. (2014). Anthropogenic and natural radiative forcing. In T. F. Stocker, et al. (Eds.), *Climate Change 2013: The Physical Science Basis. Contribution of Working Group I to the Fifth Assessment Report of the Intergovernmental Panel on Climate Change* (pp. 659–740). Cambridge, U. K., and New York: Cambridge Univ. Press. https://doi.org/10.1017/CBO9781107415324.018

Neelin, J. D., & Held, I. M. (1987). Modeling tropical convergence based on the moist static energy budget. *Monthly Weather Review*, *115*(1), 3–12. https://doi.org/10.1175/1520-0493(1987)115%3C0003:MTCBOT%3E2.0.CO;2

Oh, J.-H., Kim, K.-Y., & Lim, G.-H. (2012). Impact of MJO on the diurnal cycle of rainfall over the western Maritime Continent in the austral summer. *Climate Dynamics*, *38*(5–6), 1167–1180. https://doi.org/10.1007/s00382-011-1237-4

Palmer, K. F., & Williams, D. (1974). Optical properties of water in the near infrared. *JOSA*, *64*(8), 1107–1110. https://doi.org/10.1364/JOSA.64.001107

Peatman, S. C., Matthews, A. J., & Stevens, D. P. (2014). Propagation of the Madden-Julian Oscillation through the Maritime Continent and scale interaction with the diurnal cycle of precipitation. *Quarterly Journal of the Royal Meteorological Society*, *140*(680), 814–825. https://doi.org/10.1002/qj.2161

Platnick, S., Meyer, K. G., King, M. D., Wind, G., Amarasinghe, N., Marchant, B., et al. (2017). The MODIS cloud optical and microphysical products: Collection 6 updates and examples from Terra and Aqua. *IEEE Transactions on Geoscience and Remote Sensing*, *55*(1), 502–525. https://doi.org/10.1109/TGRS.2016.2610522

Powers, J. G., Klemp, J. B., Skamarock, W. C., Davis, C. A., Dudhia, J., Gill, D. O., et al. (2017). The Weather Research and Forecasting model: Overview, system efforts, and future directions. *Bulletin of the American Meteorological Society*, *98*(8), 1717–1737. https://doi.org/10.1175/BAMS-D-15-00308.1

Prasad, A. A., Sherwood, S. C., Reeder, M. J., & Lane, T. P. (2019). Rapidly evolving cirrus clouds modulated by convectively generated gravity waves. *Journal of Geophysical Research: Atmospheres*, *124*, 7327–7338. https://doi.org/10.1029/2019JD030538

Rauniyar, S. P., & Walsh, K. J. (2011). Scale interaction of the diurnal cycle of rainfall over the Maritime Continent and Australia: Influence of the MJO. *Journal of Climate*, *24*(2), 325–348. https://doi.org/10.1175/2010JCLI3673.1

Raymond, D. J. (2001). A new model of the Madden-Julian oscillation. *Journal of the Atmospheric Sciences*, *58*(18), 2807–2819. https://doi.org/10.1175/1520-0469(2001)058%3C2807:ANMOTM%3E2.0.CO;2

Ren, T., Yang, P., Tang, G., Huang, X., & Mlawer, E. (2020). Improved δ-Eddington approximation for optically thin clouds. *Journal of Quantitative Spectroscopy and Radiative Transfer*, *240*, 106,694. https://doi.org/10.1016/j.jqsrt.2019.106694

Rossow, W. B., & Schiffer, R. A. (1991). ISCCP cloud data products. *Bulletin of the American Meteorological Society*, *72*(1), 2–20. https://doi.org/10.1175/1520-0477(1991)072%3C0002:ICDP%3E2.0.CO;2

Ruppert, J. H. Jr., & Johnson, R. H. (2015). Diurnally modulated cumulus moistening in the preonset stage of the Madden-Julian oscillation during DYNAMO. *Journal of the Atmospheric Sciences*, *72*(4), 1622–1647. https://doi.org/10.1175/JAS-D-14-0218.1

Sakaeda, N., Kiladis, G., & Dias, J. (2017). The diurnal cycle of tropical cloudiness and rainfall associated with the Madden-Julian oscillation. *Journal of Climate*, *30*(11), 3999–4020. https://doi.org/10.1175/JCLI-D-16-0788.1

Salby, M. L., & Hendon, H. H. (1994). Intraseasonal behavior of clouds, temperature, and motion in the tropics. *Journal of the Atmospheric Sciences*, *51*(15), 2207–2224. https://doi.org/10.1175/1520-0469(1994)051%3C2207:IBOCTA%3E2.0.CO;2

Sassen, K., Wang, Z., & Liu, D. (2009). Cirrus clouds and deep convection in the tropics: Insights from CALIPSO and CloudSat. *Journal of Geophysical Research*, *114*, D00H06. https://doi.org/10.1029/2009JD011916

Schmidt, G. A., Ruedy, R., Hansen, J. E., Aleinov, I., Bell, N., Bauer, M., et al. (2006). Present-day atmospheric simulations using GISS ModelE: Comparison to in situ, satellite, and reanalysis data. *Journal of Climate*, *19*(2), 153–192. https://doi.org/10.1175/JCLI3612.1

Schmitt, C. G., & Heymsfield, A. J. (2014). Observational quantification of the separation of simple and complex atmospheric ice particles. *Geophysical Research Letters*, *41*, 1301–1307. https://doi.org/10.1002/2013GL058781

Schoeberl, M. R., Jensen, E. J., & Woods, S. (2015). Gravity waves amplify upper tropospheric dehydration by clouds. *Earth and Space Science*, *2*, 485–500. https://doi.org/10.1002/2015EA000127

Skamarock, W. C., Klemp, J. B., Dudhia, J., Gill, D. O., Barker, D. M., Duda, M. G., et al. (2008). A description of the advanced research WRF Version 3. *NCAR Technical Note NCAR/TN-475+STR* (pp. 1-96).

Slingo, A., & Slingo, J. (1988). The response of a general circulation model to cloud longwave radiative forcing. I: Introduction and initial experiments. *Quarterly Journal of the Royal Meteorological Society*, *114*(482), 1027–1062. https://doi.org/10.1002/qj.49711448209

Sobel, A., Wang, S., & Kim, D. (2014). Moist static energy budget of the MJO during DYNAMO. *Journal of the Atmospheric Sciences*, *71*(11), 4276–4291. https://doi.org/10.1175/JAS-D-14-0052.1

Sobel, A. H., & Gildor, H. (2003). A simple time-dependent model of SST hot spots. *Journal of Climate*, *16*(23), 3978–3992. https://doi.org/10.1175/1520-0442(2003)016%3C3978:ASTMOS%3E2.0.CO;2

Stan, C., Straus, D. M., Frederiksen, J. S., Lin, H., Maloney, E. D., & Schumacher, C. (2017). Review of tropical-extratropical teleconnections on intraseasonal time scales. *Reviews of Geophysics*, *55*, 902–937. https://doi.org/10.1002/2016RG000538

Stephens, G. L. (1978). Radiation profiles in extended water clouds. II: Parameterization schemes. *Journal of the Atmospheric Sciences*, *35*, 2123–2132. https://doi.org/10.1175/1520-0469(1978)035%3C2123:RPIEWC%3E2.0.CO;2

Stephens, G. L., Gabriel, P. M., & Partain, P. T. (2001). Parameterization of atmospheric radiative transfer. Part I: Validity of simple models. *Journal of the Atmospheric Sciences*, *58*(22), 3391–3409. https://doi.org/10.1175/1520-0469(2001)058%3C3391:POARTP%3E2.0.CO;2

Su, H., Jiang, J. H., Zhai, C., Perun, V. S., Shen, J. T., Del Genio, A., et al. (2013). Diagnosis of regime-dependent cloud simulation errors in CMIP5 models using "A-Train" satellite observations and reanalysis data. *Journal of Geophysical Research: Atmospheres*, *118*, 2762–2780. https://doi.org/10.1029/2012JD018575

Sui, C., & Lau, K. (1992). Multiscale phenomena in the tropical atmosphere over the western Pacific. *Monthly Weather Review*, *120*(3), 407–430. https://doi.org/10.1175/1520-0493(1992)120%3C0407:MPITTA%3E2.0.CO;2

Tang, G., Yang, P., Kattawar, G. W., Huang, X., Mlawer, E. J., Baum, B. A., & King, M. D. (2018). Improvement of the simulation of cloud longwave scattering in broadband radiative transfer models. *Journal of the Atmospheric Sciences*, *75*(7), 2217–2233. https://doi.org/10.1175/JAS-D-18-0014.1

Tian, B., Waliser, D. E., Fetzer, E. J., Lambrigtsen, B. H., Yung, Y. L., & Wang, B. (2006). Vertical moist thermodynamic structure and spatial-temporal evolution of the MJO in AIRS observations. *Journal of the Atmospheric Sciences*, *63*(10), 2462–2485. https://doi.org/10.1175/JAS3782.1

Trier, S. B., & Sharman, R. D. (2016). Mechanisms influencing cirrus banding and aviation turbulence near a convectively enhanced upper-level jet stream. *Monthly Weather Review*, *144*(8), 3003–3027. https://doi.org/10.1175/MWR-D-16-0094.1

Tsushima, Y., Ringer, M. A., Webb, M. J., & Williams, K. D. (2013). Quantitative evaluation of the seasonal variations in climate model cloud regimes. *Climate Dynamics*, *41*(9–10), 2679–2696. https://doi.org/10.1007/s00382-012-1609-4

Tung, W.-E., Giannakis, D., & Majda, A. J. (2014). Symmetric and antisymmetric convection signals in the Madden-Julian Oscillation. Part I: Basic modes in infrared brightness temperature. *Journal of the Atmospheric Sciences*, *71*(9), 3302–3326. https://doi.org/10.1175/JAS-D-13-0122.1

Ueyama, R., Jensen, E. J., Pfister, L., & Kim, J. E. (2015). Dynamical, convective, and microphysical control on wintertime distributions of water vapor and clouds in the tropical tropopause layer. *Journal of Geophysical Research: Atmospheres*, *120*, 10,483–10,500. https://doi.org/10.1002/2015JD023318

Vignesh, P. P., Jiang, J. H., Kishore, P., Su, H., Smay, T., Brighton, N., & Velicogna, I. (2020). Assessment of CMIP6 cloud fraction and comparison with satellite observations. *Earth and Space Science*, *7*, e2019EA000975. https://doi.org/10.1029/2019EA000975

Vincent, C. L., & Lane, T. P. (2016). Evolution of the diurnal precipitation cycle with the passage of a Madden-Julian Oscillation event through the Maritime Continent. *Monthly Weather Review*, *144*(5), 1983–2005. https://doi.org/10.1175/MWR-D-15-0326.1

Vincent, C. L., & Lane, T. P. (2017). A 10-year austral summer climatology of observed and modeled intraseasonal, mesoscale, and diurnal variations over the Maritime Continent. *Journal of Climate*, *30*(10), 3807–3828. https://doi.org/10.1175/JCLI-D-16-0688.1

Wang, H., & Su, W. (2013). Evaluating and understanding top of the atmosphere cloud radiative effects in Intergovernmental Panel on Climate Change (IPCC) Fifth Assessment Report (AR5) Coupled Model Intercomparison Project Phase 5 (CMIP5) models using satellite observations. *Journal of Geophysical Research: Atmospheres*, *118*, 683–699. https://doi.org/10.1029/2012JD018619

Wheeler, M. C., & Hendon, H. H. (2004). An all-season real-time multivariate MJO index: Development of an index for monitoring and prediction. *Monthly Weather Review*, *132*(8), 1917–1932. https://doi.org/10.1175/1520-0493(2004)132%3C1917:AARMMI%3E2.0.CO;2

Wilber, A. C., Kratz, D. P., & Gupta, S. K. (1999). *Surface emissivity maps for use in satellite retrievals of longwave radiation*. Hampton, VA: NASA Langley Research Center.

Williams, E., & Stanfill, S. (2002). The physical origin of the land-ocean contrast in lightning activity. *Comptes Rendus Physique*, *3*(10), 1277–1292. https://doi.org/10.1016/s1631-0705(02)01407-x

Wing, A. A., Emanuel, K., Holloway, C. E., & Muller, C. (2017). Convective self-aggregation in numerical simulations: A review. *Surveys in Geophysics*, *38*(6), 1173–1197. https://doi.org/10.1007/s10712-017-9408-4

Yang, P., Bi, L., Baum, B. A., Liou, K.-N., Kattawar, G. W., Mishchenko, M. I., & Cole, B. (2013). Spectrally consistent scattering, absorption, and polarization properties of atmospheric ice crystals at wavelengths from 0.2 to 100 $\mu$m. *Journal of the Atmospheric Sciences*, *70*(1), 330–347. https://doi.org/10.1175/JAS-D-12-039.1

Zhang, B., Kramer, R. J., & Soden, B. J. (2019). Radiative feedbacks associated with the Madden-Julian Oscillation. *Journal of Climate*, *32*(20), 7055–7065. https://doi.org/10.1175/JCLI-D-19-0144.1

Zhang, C. (2005). Madden-Julian Oscillation. *Reviews of Geophysics*, *43*, RG2003. https://doi.org/10.1029/2004RG000158

Zhang, C. (2013). Madden-Julian Oscillation: Bridging weather and climate. *Bulletin of the American Meteorological Society*, *94*(12), 1849–1870. https://doi.org/10.1175/BAMS-D-12-00026.1

Zhang, C., & Dong, M. (2004). Seasonality in the Madden-Julian Oscillation. *Journal of Climate*, *17*(16), 3169–3180. https://doi.org/10.1175/1520-0442(2004)017%3C3169:SITMO%3E2.0.CO;2

Zhang, C., & Ling, J. (2017). Barrier effect of the Indo-Pacific Maritime Continent on the MJO: Perspectives from tracking MJO precipitation. *Journal of Climate*, *30*(9), 3439–3459. https://doi.org/10.1175/JCLI-D-16-0614.1